land

MDPI

Article

Remote Sensing and Field Measurements for the Analysis of the Thermal Environment in the "Bosco Verticale" Area in Milan City

Georgios Kalogeropoulos [1,*], Julia Tzortzi [2,*] and Argiro Dimoudi [1]

[1] Department of Environmental Engineering, Democritus University of Thrace, 671 00 Xanthi, Greece; adimoudi@env.duth.gr
[2] Department ABC Architecture, Built Environment and Construction Engineering, 20133 Milano, Italy
* Correspondence: gkaloge@env.duth.gr (G.K.); julia.georgi@polimi.it (J.T.)

Abstract: The trend of urbanization nowadays has caused serious issues related to climate. One of the most important ones is that of the 'Urban Heat Island (UHI)' and it occurs in major cities throughout the world. The most important categories, and therefore the most studied ones, are the canopy urban heat island (CUHI) and surface heat island (SUHI). The aim and the novelty of the current study was to assess different remote sensing approaches to detect the thermal environment of an open area inside a large city. The study was undertaken in an urban area with green spaces, in the Bosco Verticale area in the city of Milan, during the spring and summer period of 2021. The area is characterized by different types of cover materials, which were investigated in terms of surface temperature under shaded and non-shaded conditions. Both field measurements and remote sensing techniques were applied. Remote sensing techniques included downscaling techniques and the usage of different split-window algorithms applied on the Landsat8 satellite sensor data. The land surface temperature (LST) extracted from remote sensing methods was compared with the surface temperature derived from in situ measurements. For the needs of the study, both in situ measurements and the collection of meteorological data from different fixed meteorological stations throughout the city of Milan were carried out. The results revealed the significance of greenery presence inside the urban environment, as a comparison of the meteorological data across the urban area of Milan showed that the areas with a low presence of greenery were found to be warmer than those with a higher presence of green elements. Concerning the field measurements in the study area, the results showed a significant reduction in both surface and air temperature in shaded places. On the other hand, the presence of conventional artificial materials in sunny areas led to relatively high values of both surface and air temperature. The downscaling method showed satisfying results in terms of average LST values; however, some discrepancies appeared in terms of the RMSE index. The application of split-window algorithms has shown that some forms of the 'Generalized split-window algorithm' and some forms of the 'Jimenez-Munoz algorithm' presented better performance among the studied algorithms. Comparing the LST values derived from the most representative algorithm, the 'Du, Wan algorithm', with those derived from downscaling methods, it was found to be quite close. However, under shaded conditions, the results derived from the 'Split-window algorithm' were found to be more precise. The application of remote sensing techniques in microscale in urban regions should be further studied in future, as they could be an essential tool for observing microclimatic conditions in urban areas and on building scale.

Keywords: remote sensing; downscaling LST; split-window algorithms; field measurements

check for updates

Citation: Kalogeropoulos, G.; Tzortzi, J.; Dimoudi, A. Remote Sensing and Field Measurements for the Analysis of the Thermal Environment in the "Bosco Verticale" Area in Milan City. *Land* **2024**, *13*, 182. https://doi.org/10.3390/land13020182

Academic Editor: Chuanrong Zhang

Received: 12 December 2023
Revised: 23 January 2024
Accepted: 31 January 2024
Published: 3 February 2024

Copyright: © 2024 by the authors. Licensee MDPI, Basel, Switzerland. This article is an open access article distributed under the terms and conditions of the Creative Commons Attribution (CC BY) license (https://creativecommons.org/licenses/by/4.0/).

1. Introduction

One of the most important issues nowadays is that of the urban heat island effect (UHI) [1], and the land surface temperature [2] is very crucial for the assessment of this phe-

nomenon. UHI describes a situation when the air temperature inside the city core is higher than that of suburban areas [3]. Mainly, there are four categories of the phenomenon [4]:

- Surface (SUHI)
- Subsurface
- Canopy layer (CUHI)
- Boundary (BUHI)

However, due to the monitoring method (Subsurface and BUHI ones are very complicated in terms of observation), the SUHI and CUHI are the most observed ones. The CUHI effect is usually observed by comparing the air temperature inside the city core with that observed in rural areas. In situ measurements with mobile stations usually take place and software modeling in many cases is also applied [5,6]. There are a lot of computer software models, based on computational fluid dynamics (CFD models), that have the ability to calculate different microclimatic parameters at every point of the meshed space with high accuracy [7]. Although both mobile and meteorological stations usually offer information about microclimate effects inside urban environments, in many cases they fail to provide detailed data about the spatial distribution of the air temperature inside cities [8].

On the other hand, the SUHI effect is usually observed with remote sensing techniques. Satellite data provide detailed data about the land surface temperature (LST) in large spatial coverage [9,10]. There are a lot of LST products that are widely applied to climate change issues, urban microclimates, hydrology and surface energy balance [11,12]. Different satellite products are globally used for urban heat island analysis, such as 'Landsat' [13,14], Sentinel [15,16], the 'Advanced Spaceborne Thermal Emission and Reflection Radiometer (ASTER)' [17], the 'MODerate resolution Imaging Spectroradiometer (MODIS)' [18], the 'Advanced Very High Resolution Radiometer (AVHRR)' [19] and the 'ENVIronment SATellite (ENVISAT)' [18].

The current study investigated the ability of remote sensing methods to calculate the land surface temperature (LST) inside the urban environment, at a microscale level and more specifically at the level of building scale according to climatological scales [20]. According to climatological scales, the building level is considered as a small part of an urban area. As previously mentioned, remote sensing techniques have been tested in urban environments; however, their accuracy in small parts of urban environments is rather limited. In the current study, these methods were investigated, with a comparison of the land surface temperature (LST) extracted remotely from satellite sensors against the surface temperature derived from field measurements. More specifically, downscaling methods and also several LST algorithms in the Landsat8 sensor were both applied, and their performance inside an urban complex environment was investigated. The examined area was the Bosco Verticale area, which is located inside the city of Milan, Northern Italy. More specifically, the selected area lies in the region of Puorta Nuova Isola, which is an area that has been recently transformed into an urban district. Apart from the fact that it is a broad area and therefore an ideal area for the application of remote sensing methods, the current area has also drawn the interest of the scientific community, mainly because of the two tall residential buildings that house trees as a vertical forest architecture design [21]. By the time the project had been completed in the selected area, it was the first time in situ measurements took place to assess the microclimatic conditions of the broader area. So, apart from the evaluation of remote sensing techniques, the current study aimed to evaluate the microclimatic conditions in an area that hosts a special green structure and a lot of visitors and facilities on a daily basis.

The field measurements were conducted during the spring and summer period of the year of 2021 (May to August). The microclimatic parameters of surface temperature, air temperature and relative humidity were monitored. Multiple measurement points, representing different groundcover materials, were selected along the study area, and the microclimatic parameters were investigated under shaded and non-shaded conditions. The parameter of surface albedo was also investigated with remote sensing methods. Microclimatic parameters were also acquired from six weather stations across the urban

area of Milan, and the derived values were compared with those collected from field measurements that took place in the study area. Simultaneously, satellite data were acquired during the measurement period, and both the downscaling method and a number of LST algorithms applied to the Landsat8 sensor were evaluated.

2. Study Area—Methodology

2.1. Study Area

The Bosco Verticale area in Milan city, Northern Italy, was studied. This area was selected because it is an open urban area, with various cover-type materials and extensive green surfaces on buildings. In the area, there are two residential towers covered with extensive greenery in the form of vertical forestry, an urban heat island mitigation approach of urban greenery that attracts scientific and architectural interest and also visitors to observe it. Figure 1a presents a panoramic view of the area. The study area covers 18,665.9 m^2. There are 6 types of cover materials in outdoor areas (Figure 1b–g): pavement concrete tiles (4917.8 m^2), narrow sand roads (2187.5 m^2), grass (6778.8 m^2), rubber (515.4 m^2), granite-paved roads (3296 m^2) and narrow concrete roads (969.9 m^2) (Figure 2a).



(**a**)

Figure 1. *Cont.*

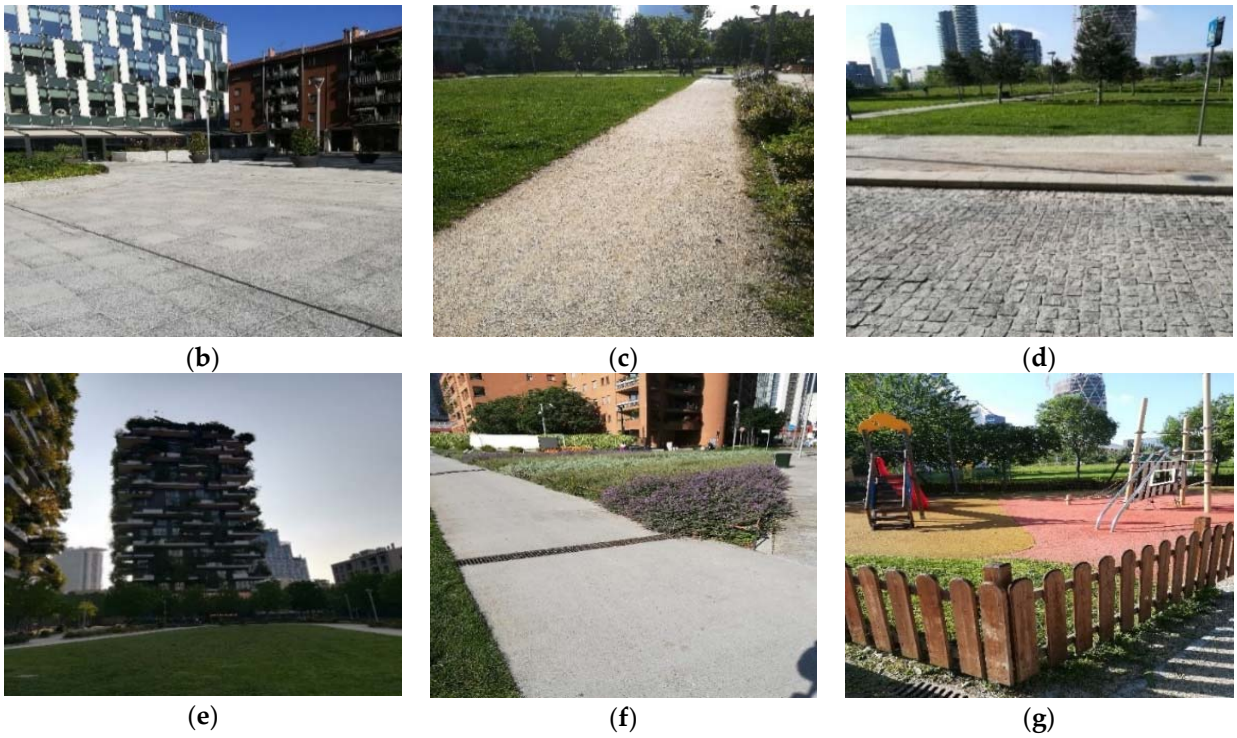

(**b**) (**c**) (**d**)

(**e**) (**f**) (**g**)

Figure 1. (**a**) Satellite view of the study area (QGIS). (**b**) Pavement concrete tiles (personal photo). (**c**) Narrow sand roads (personal photo). (**d**) Paved road (personal photo). (**e**) Grass (personal photo). (**f**) Narrow concrete roads (personal photo). (**g**) Rubber (personal photo).

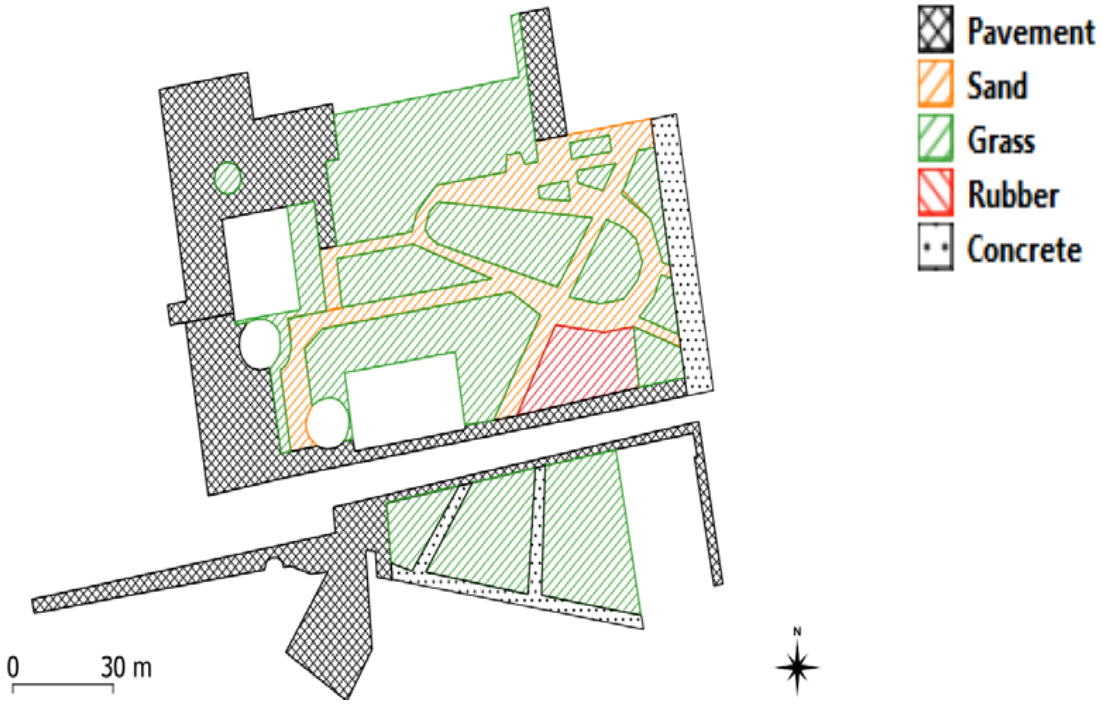

(**a**)

Figure 2. *Cont.*

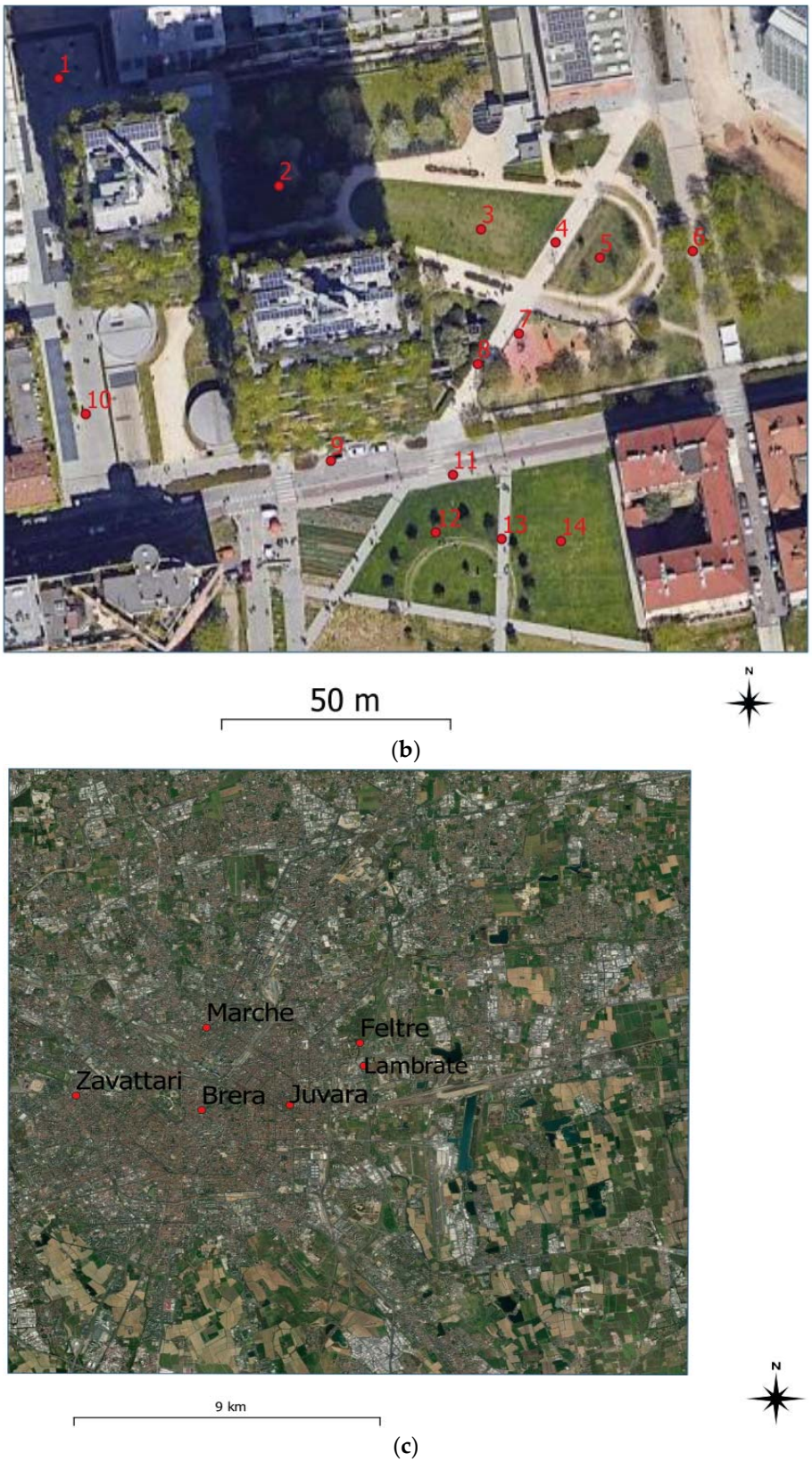

Figure 2. (**a**) The cover-type materials in the study area. (**b**) The measurement points (1–14) in the study area. (**c**) Weather stations' locations in the city (QGIS).

2.2. Methodology

The current study aimed to do the following: (i) investigate microclimatic parameters in the area of Bosco Verticale in Milan city and (ii) assess the efficiency of remote sensing techniques for the estimation of surface temperature inside complicated urban environments. In situ measurements, the collection of microclimatic parameters from weather meteorological stations and remote sensing techniques took place. Surface temperature, air temperature and relative humidity were the microclimatic parameters that were measured and assessed at 14 points in the area (Figure 2b). An infrared thermometer (IR) and a thermal camera (TC) were used in the measurements. The infrared thermometer was selected due to its handling simplicity, as it has the ability of collecting multiple parameters, such as air temperature, relative humidity and surface temperature. The thermal camera was selected as it offers more surface temperature data. Detailed information about the measuring instruments are presented in Section 2.2.

Sun exposure was also investigated in the current study, and therefore the microclimatic parameters were evaluated in shaded and non-shaded places. Also, both the air temperature and relative humidity measured data in the area were compared with the ones gathered from weather stations throughout Milan city to investigate differences with the study area. In total, six meteorological stations were located across the city of Milan in Brera, Lambrate, Zavattari, Feltre, Juvara and Marche (Figure 2c).

The efficiency of remote sensing techniques for the estimation of surface temperature inside complicated urban environments was also assessed. Downscaling techniques and a number of Landsat8 LST split-window algorithms were both applied, and their applicability was investigated on a building scale inside a large urban environment. Concerning the downscaling method, the sharpening thermal imagery (TsHARP) method was used [22]. The TsHARP method was applied because it had already shown satisfactory results in the disaggregation procedure from MODIS to the Landsat8 sensor [23], and it is an accurate method in urban environments [24]. In the current study, the ability of the TsHARP method was assessed in the urban environment on a building scale. Figure 3 describes the methodology approach that was followed in order the low-resolution LST data that were provided from MODIS products could be downscaled to the high-resolution ones of the Setinel-2 sensor. Accordingly, Figure 4, describes the methodology by which low-resolution data were downscaled to the high-resolution ones of the Landsat8 sensor. As can be seen in both Figures 3 and 4, the TsHARP method relies on the reverse relationship between the 'normalized difference vegetation index (NDVI)' (a spectral index that is explained in Section 2.5) and the 'land surface temperature (LST)' [25,26]. The whole process of the thermal sharpening of the LST data took place in the RStudio tool [27]. Another tool that was included in the current study was the QGIS [28]. The field measurement points were represented in the QGIS tool and, as vector points, were used in order that the derived LST parameter could be extracted from those vector points with the RStudio packages. The final high-resolution LST data were compared with the ones derived from in situ measurements in terms of statistical indices, as both the 'Root mean square index (RMSE)' and the 'Coefficient of determination (R^2) were elected as validation statistical tools. More details about the products that were used for the downscaling method are presented in Section 3.3.2.

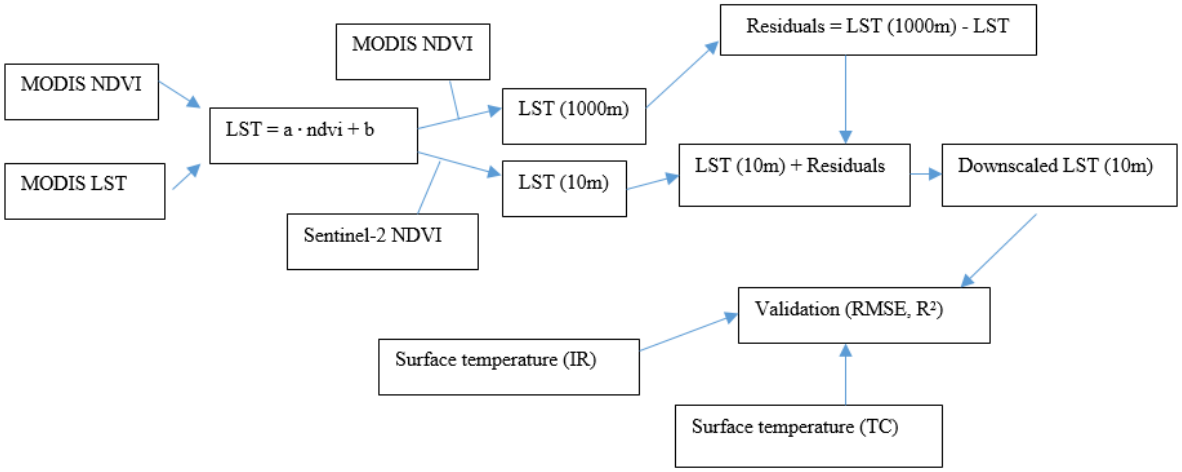

Figure 3. Flowchart of the downscaling technique of the LST images from 1000 m spatial resolution (MODIS) to 10 m (Sentinel-2).

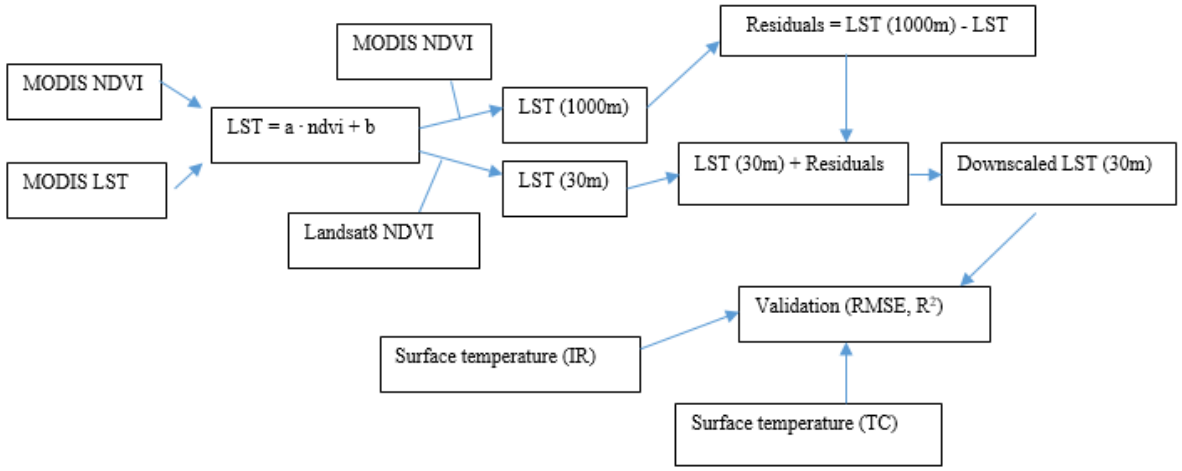

Figure 4. Flowchart for the downscaling technique of the LST images from 1000 m spatial resolution (MODIS) to 30 m (Landsat8).

Concerning the Landsat8 LST algorithms, 12 split-window algorithms were applied and evaluated. The 'split window algorithms' were applied as previous studies have shown that they are able to quantify the LST parameter accurately in every atmospheric condition [29]. The more suitable one (in terms of RMSE and R^2) is indicated for the urban area of Milan. More analytically, in Section 3.3.1., the estimation of the Landsat8 LST algorithms is described. Sun exposure analysis and surface reflectance analysis also took place in the current study, in order for the ability of both remote sensing methods to detect shading parts and surface conditions on a building level to be assessed. The methodology and the albedo coefficient derived from the Landsat8 bands are presented in detail in Section 2.4.

2.3. In Situ Measurements and Microclimatic Data

The microclimatic parameters air temperature (Tair) and relative humidity (RH), and also the surface temperature (Tsurface), were measured. The measurements took place in the period from 19 May 2021 to 20 August 2021, between 10:00 to 14:00, with 30 minutes' time step. The selected period is considered as a period with clear sky and warm conditions. In fact, during the measurement period, cloudless sky conditions prevailed, which facilitated the selection of satellite images and the study of heat stress conditions in the city of Milan during the summer period. For this reason, pavement concrete tiles, narrow

sand roads, grass, rubber and narrow concrete roads were selected for measurements, as it was considered that those areas are used by citizens. Figure 2a presents the area of interest as it was designed in GIS.

Two measurement instruments were included in the current study: a MESTEK infrared thermometer IR 01 D that measures Tair, RH and Tsurface and a thermal camera (TC) HT–A1 for surface temperature (Tsurface) measurements. Concerning Tsurface, in both instruments, the emissivity coefficient was set to 0.95 as measurements were conducted in an outdoor environment. Totally, 14 measurement points were selected across the study area (Figure 2b). The measurement time at each point did not exceed 5 min, in order for the collected data to be compared with the LST parameter that was extracted from satellite sensors.

2.4. Downscaling LST Images

In the current study, the downscaling of LST data took place. This 'downscaling "method"' refers to quality improvement of the LST data in terms of spatial resolution. As has already mentioned in Section 2.2, the whole procedure is based on the reverse relationship between the LST and NDVI index.

Concerning the availability of remote sensing data for the downscaling method, in total, 6 Landsat8, 9 Sentinel-2 and 24 MODIS clear images were identified during the measurement period and included in the analysis. The MODIS sensor was selected as its data are available multiple times per day. More specifically, in the current study, the MOD11A1 data were available at 10:30 am and the MYD11A1 data were available at 13:30 pm every day. For this reason, the in situ measurements started half an hour before the passing over of the MOD11A1 product and half an hour after the passing over of the MYD11A1, in order to ensure the availability of MODIS satellite data. From both the MOD11A1 and MYD11A1, the LST parameter was extracted and the "EPSG:32632—WGS 84/UTM zone 32N" was selected as a coordinate reference system, as it is the same coordinate system for both the Sentinel-2 and Landsat8 sensors. At the same time, the MOD09GQ and MYD09GQ products were also downloaded in order, so that both the NIR and RED bands of the MODIS satellite could be retrieved. Both the NIR and RED MODIS bands were reprojected and then multiplied by 0.0001, which is the scaling factor according to the guidelines. All MODIS data were downloaded from the [30] webpage.

Both the Landsat8 and Sentinel-2 sensors were selected because they offer information with a relatively high spatial resolution of 30 m and 10 m, respectively. Sentinel-2 sensor offers relatively high-quality data from two platforms, S2A and S2B, each one of them passing over every 10 days, enabling in that way the availability of satellite data every 5 days [31]. Thus, it offers the ability of conducting the TsHARP method from 1000 m (MODIS) to 10 m (Sentinel-2), which was adapted to the current study [22]. The Sentinel-2 data were acquired from the [32] webpage. Both the NIR and RED bands from the Sentinel-2 sensor were multiplied by 0.0001 as well, which is the scale factor acquired from metadata files. On the other hand, the Landsat8 satellite offers data every 7 days and also contains thermal infrared channel spectral information in two channels (band 10 and band 11), enabling in that way the authors to apply the downscaling method and calculate the land surface temperature (LST). The Landsat8 satellite data were acquired from the [33] webpage. The TsHARP method was applied because it had already shown satisfactory results in the case of the disaggregation procedure from MODIS to the Landsat8 sensor [23]. All available remote sensing data that were included in the current study are presented in Table 1.

Table 1. Satellite products used in the current study.

Date	Sensor						
	MODIS				Sentinel-2		Landsat8
	MOD11A1	MYD11A1	MOD09GQ	MYD09GQ	S2A	S2B	
19 May 2021							
21 May 2021							
26 May 2021							
28 May 2021							
31 May 2021							
10 June 2021							
13 June 2021							
25 June 2021							
29 June 2021							
30 June 2021							
10 July 2021							
20 July 2021							
22 July 2021							
9 August 2021							
16 August 2021							

Each color represents the available satellite dataset of each sensor.

2.5. Land Surface Temperature Estimation

A number of split-window algorithms that are widely used were included in the current study. For the estimation of the LST, in many cases, the emissivity value of both bands (10 and 11) must be calculated [34]. In the current study, a number of split-window algorithms applied to Landsat8 were tested and the most applicable one in urban environments is indicated.

2.5.1. Enterprise Algorithm

A widely used equation is the 'enterprise algorithm', expressed as follows [35,36]:

$$LST = C_0 + C_1 \cdot BT_{10} + C_2 \cdot (BT_{10} - BT_{11}) + C_3 \cdot \varepsilon + C_4 \cdot \varepsilon \cdot (BT_{10} - BT_{11}) + C_5 \cdot \Delta\varepsilon \quad (1)$$

where

- C_i ($i = 0 \sim 5$), algorithm coefficients;
- BT_{10} and $BT_{11,}$ the Landsat 8 brightness temperatures for both channels 10 and 11 respectively;
- ε, the mean land surface emissivity (LSE) ($\varepsilon = 0.5 \times (\varepsilon_{10} + \varepsilon_{11})$);
- $\Delta\varepsilon$, the land surface emissivity difference of thermal bands ($\Delta\varepsilon = \varepsilon_{10} - \varepsilon_{11}$).

The brightness temperature (BT) can be derived using the Planck equation [37]:

$$BT = K_2 / \left[\ln \left(\frac{K_2}{K_1 / L_\lambda} + 1 \right) \right] \quad (2)$$

where

- BT, the recorded radiant temperature on sensor surface (K);
- L_λ, the spectral radiation ($w/(m^2 ster\ \mu m)$);
- K_1 ($w/(m^2 ster\ \mu m)$) and K_2 (K) are both calibration constants ($w/(m^2 ster\ \mu m)$), the K_1 values are estimated as 774.89 and 480.89 ($w/m^2 ster\ \mu m$) for band 10 and band 11 and the K_2 values as 1321.08 and 1201.14 (K) for band 10 and 11, respectively.

The spectral radiance L_λ is calculated as follows:

$$L_\lambda = M_L \cdot Q_{cal} + A_L \quad (3)$$

where

- M_L, the band-specific multiplicative factor derived from the metadata file;
- A_L, the band-specific additive factor also acquired from the metadata file;
- Qcal, quantized and calibrated pixel values of the specific band.

The land surface emissivity (LSE) estimation is based on the NDVI Thresholds Method [25,26] and is calculated as follows:

$$LSE = \varepsilon_s \cdot (1 - FVC) + \varepsilon_v \cdot FVC \quad (4)$$

where

- $\varepsilon_{v,}$ the vegetation emissivity, considered 0.987 for TIRS1 and 0.989 for TIRS2;
- ε_s, the soil emissivity, considered 0.971 for TIRS1 and 0.977 for TIRS2. These values are obtained from the STER spectral Library [38,39];
- FVC, the fractional vegetation cover, is calculated from the following equation:

$$FVC = \left(\frac{NDVI - NDVI_s}{NDVI_v - NDVI_s} \right)^2 \quad (5)$$

where

- $NDVI_{s,}$ the NDVI index for soil areas;
- $NDVI_{v,}$ the NDVI index for vegetated areas. A typical value of NDVI for bare soils and dense vegetation is 0.2 and 0.9, respectively [40,41].

The NDVI index is calculated as follow [25,26]:

$$NDVI = \left(\frac{NIR - RED}{NIR + RED} \right) \quad (6)$$

where

- NIR, the near-infrared band;
- RED, the red band.

2.5.2. Generalized Split-Window Algorithm

Another commonly used algorithm for the estimation of LST is the 'Generalized split-window algorithm' developed by Wan and Dozier, 1996, and expressed as follows [42]:

$$LST = C_0 + \left(C_1 + C_2 \cdot \frac{1-\varepsilon}{\varepsilon} + C_3 \cdot \frac{\Delta\varepsilon}{\varepsilon^2} \right) \cdot \frac{BT_{10} + BT_{11}}{2} + \left(C_4 + C_5 \cdot \frac{1-\varepsilon}{\varepsilon} + C_6 \cdot \frac{\Delta\varepsilon}{\varepsilon^2} \right) \cdot \frac{BT_{10} - BT_{11}}{2} + C_7 \cdot (BT_{10} - BT_{11})^2 \quad (7)$$

2.5.3. Jimenez-Munoz Algorithm

Equation (8) presents the 'Split window algorithm' initially proposed by Sobrino et al. [25] and later elaborated by Jimenez-Munoz et al. [29]:

$$LST = BT_{10} + C_0 + C_1 \cdot (BT_{10} - BT_{11}) + C_2 \cdot (BT_{10} - BT_{11})^2 + (C_3 + C_4 \cdot w) \cdot (1 - \varepsilon) + (C_5 + C_6 \cdot w) \cdot \Delta\varepsilon \quad (8)$$

where

- w is the atmospheric vapor ($g \cdot cm^{-2}$ or $kg \cdot m^{-2}$).

The atmospheric vapor is calculated by the Modified Split-Window Covariance and Variance Ratio (MSWCVR) according to [43,44]:

$$wv = -9.674 \cdot \left(\frac{\tau_i}{\tau_j}\right)^2 + 0.653 \cdot \left(\frac{\tau_i}{\tau_j}\right) + 9.087 \quad (9)$$

where

- τ, the band effective atmospheric transmittance;
- τ_i/τ_j fraction is calculated as follows:

$$\frac{\tau_i}{\tau_j} = \frac{\varepsilon_i}{\varepsilon_j} R_{i,j} \quad (10)$$

$R_{i,l}$ is calculated from the following equation:

$$R_{i,j} = \frac{\sum_{k=1}^{N} \left(BT_{10} - \overline{BT_{10}}\right) \cdot \left(BT_{11} - \overline{BT_{11}}\right)}{\sum_{k=1}^{N} \left(BT_{10} - \overline{BT_{10}}\right)^2} \quad (11)$$

where

- N is the number of adjacent pixels.

The values of the split-window algorithm coefficients are presented in Table 2.

Table 2. Values of the split-window algorithm coefficients.

	Enterprise		Generalized		Jimenez-Munoz	
No.	**1a**	**2a**	**3b**	**4c**	**5a**	**6d**
C0	67.297 [a]	−2.64 [a]	−0.41165 [b]	2.2925 [c]	−0.717 [a]	−0.268 [d]
C1	0.985 [a]	1.012 [a]	1.00522 [b]	0.9929 [c]	1.988 [a]	1.378 [d]
C2	−6.916 [a]	0.142 [a]	0.14543 [b]	0.1545 [c]	0.121 [a]	0.183 [d]
C3	−63.855 [a]	−0.201 [a]	0.27297 [b]	−0.3122 [c]	70.148 [a]	54.30 [d]
C4	9.548 [a]	2.844 [a]	4.06655 [b]	3.7186 [c]	−7.006 [a]	−2.238 [d]
C5	−90.919 [a]	−0.569 [a]	6.92512 [b]	0.3502 [c]	−143.246 [a]	−129.20 [d]
C6	-	−7.6 [a]	18.27461 [b]	−3.5889 [c]	19.247 [a]	16.40 [d]
C7	-	0.263 [a]	0.24468 [b]	0.1825 [c]	-	-

[a] [45], [b] [46], [c] [47], [d] [29].

2.5.4. Other Split-Window Algorithms

Apart from the 'enterprise' (Equation (1)), the 'generalized' (Equation (7)) and the 'developed algorithm by Jimenez and Munoz (Equation (8)), various split-window algorithms were also used in the current study, and they are presented in Table 3.

Table 3. List of other split-window algorithms (Equations (12)–(17)) included in the current study.

Algorithms	**Equation No.**
$LST = 0.39 \cdot BT_{10}^2 + BT_{10} - 0.78 \cdot BT_{10} \cdot BT_{11} - 1.34 \cdot BT_{11} - 1.34 \cdot BT_{11} + 0.39 \cdot BT_{11}^2 + 0.56$	(12) [a]
$LST = BT_{10} \cdot (0.5 \cdot P_v + 3.1) + BT_{11} \cdot (-0.5 \cdot P_v - 2.1) - 5.5 \cdot P_v + 3.1$	(13) [b]
$LST = 1.035 \cdot BT_{10} + 3.046 \cdot (BT_{10} - BT_{11}) - 10.93$	(14) [c]
$LST = [BT_{10} + 3.33 \cdot (BT_{10} - BT_{11})] \cdot \left(\frac{5.5 - \varepsilon_{10}}{4.5}\right) + 0.75 \cdot BT_{11} \cdot \Delta\varepsilon$	(15) [d]
$LST = BT_{10} + 1.06 \cdot (BT_{10} - BT_{11}) + 0.46 \cdot (BT_{10} - BT_{11})^2 + 53 \cdot (1 - \varepsilon_{10}) - 53 \cdot (\varepsilon_{10} - \varepsilon_{11})$	(16) [e]
$LST = BT_{10} + 3 \cdot (BT_{10} - BT_{11}) - 52.45 \cdot \varepsilon + 51.57$	(17) [f]

[a] [48], [b] [49], [c] [50], [d] [51], [e] [52], [f] [53].

2.6. Ground Surface Albedo Assesment

The albedo parameter (α_{short}) is also remotely assessed in the current study. The TM/ETM+ algorithm is used in the current study and is applied to Landsat8 [54]:

$$\alpha_{short} = 0.365 \cdot BLUE + 0.130 \cdot RED + 0.373 \cdot NIR + 0.085 \cdot SWIR1 + 0.072 \cdot SWIR2 - 0.0018 \quad (18)$$

where

- BLUE, the blue band;
- SWIR1 and SWIR2, the short-wave infrared bands 1 and 2, respectively.

All Landsat8 thermal bands are converted from digital numbers (DN) to top-of-atmosphere (TOA) reflectance as follows:

$$\rho_\lambda{}' = M_p \cdot Q_{cal} + A_p \quad (19)$$

where

- M_p, the band-specific multiplicative rescaling factor, acquired from the metadata files;
- A_p, the band-specific additive rescaling factor, derived from the metadata files.

Finally, the TOA reflectance (ρ_λ), with the correction of the sun angle, is estimated from the following equation:

$$\rho_\lambda = \frac{\rho_\lambda{}'}{\sin(\theta_{SE})} \quad (20)$$

where

- θ_{SE}, the local elevation sun angle.

The values of the ground material surface albedo coefficient estimated from the previously presented equations were compared with the surface albedo values acquired from the literature review and the results are presented in the following Section 3.

3. Results

3.1. In Situ Measurements

Table 4 presents the average value of each measured parameter: air temperature, air relative humidity and surface temperature. As can be seen, the average value of the air temperature, derived from the in situ measurements, was found to be equal to 31.9 °C, and the average value of the relative humidity was found to be equal to 34.7%. Concerning the surface temperature, no differences were observed in the average value and the maximum values derived from the infrared thermometer and those derived from the thermal camera (Table 5). However, there is a difference of 11.8 °C between the maximum values of surface temperature derived from the two measurement instruments in grass areas.

Table 4. Total average value of measured microclimatic parameters in the Bosco Verticale area.

Parameter (Unit)	Value
Air temperature (°C)	31.9
Relative humidity (%)	34.7
Surface temperature, IR (°C)	33.7
Surface temperature, TC (°C)	33.7

Table 5. Average and maximum values of surface temperature for different cover surface materials as measured in the Bosco Verticale area with the infrared thermometer (IR) and the thermal camera (TC).

Surface	IR		TC	
	Average (°C)	Max (°C)	Average (°C)	Max (°C)
Pavement tile	36.9	58	36.5	56.5
Sand	30.9	52.5	29.4	49.8
Grass	29.1	54.6	30.9	42.8
Rubber	48.5	62.1	47.8	65.3
Concrete	37.4	54.8	36.8	52.7

Concerning surface cover material, the red rubber presented the higher surface temperature values. Also, dark gray pavement tiles and gray concrete roads appeared to have high surface temperature values as well. On the other hand, low surface temperatures were observed in both grass and sand surfaces. In Figure 5a–c, the surface temperature (both IR and TC) and the air temperature in both shaded and sunny places are presented. As can be seen, the average surface temperature decreased in shadow areas by 15.7 °C (in the case of the IR instrument) and 13.7 °C (in the case of the TC instrument). Concerning air temperature, in shaded places, the average value was found to be equal to 30.4 °C, whereas in places that were exposed to solar radiation, the average value of the air temperature was found to be 32.4 °C, underlying in that way the significance of shading materials (either artificial or natural) to thermal environments that host a large number of visitors.

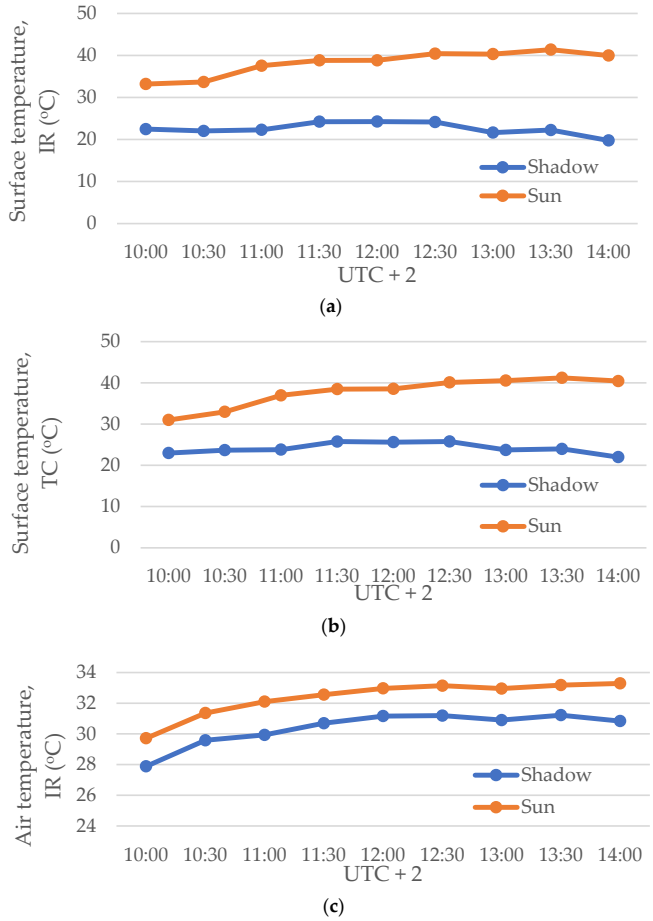

Figure 5. Average hourly temperature values in both shaded and exposed-to-the-sun areas: (**a**) surface temperature with IR instrument; (**b**) surface temperature with TC instrument; (**c**) air temperature with IR instrument.

3.2. Fixed Meteorological Stations

Data of both air temperature and relative humidity from various meteorological stations inside the city of Milan were also gathered, in Brera, Lambrate, Zavattari, Feltre, Juvara and Marche (Figure 2c). Table 6 presents the total average values of the air temperature and relative humidity from the meteorological stations inside the city of Milan. The NDVI index of the areas where the meteorological stations were located was calculated and is also presented in Table 6.

Table 6. Average values of the air temperature, the relative humidity and the NDVI index of the meteorological stations' location area.

Meteorological Station	Air Temperature (°C)	Relative Humidity (%)	NDVI
Brera	26.6	44.7	0.34
Lambrate	28.1	42.7	0.28
Zavattari	28.5	45.3	0.17
Feltre	27.7	- [a]	0.31
Juvara	26.9	43.5	0.17
Marche	27.2	43.9	0.1

[a] Data were not available.

Differences were detected between the Bosco Verticale and the various areas where the meteorological stations were located in terms of both air temperature and relative humidity. As can be noticed, the air temperature that was measured in the Bosco Verticale area was found to be 5.3 °C warmer than that of the area of Brera (lower total average temperature) and 3.4 °C warmer than that of the area of Zavattari (higher total average temperature). Also, great differences were detected in the relative humidity, as the average value that was acquired in the Bosco Verticale area was found to be equal to 34.7%. On the other hand, the average value of the relative humidity derived from the meteorological stations was found to be between 42.7% and 65.3%. These great differences may be attributed to the different measuring heights (approximately 1.5 m above ground in the case of the Bosco Verticale area and the height of the meteorological stations across the city of Milan). Also, the different measurement sensors could produce differences concerning the comparison of climatic data. Thus, the great differences that appeared between the microclimatic data gathered from in situ measurements and those derived from fixed stations should be further investigated.

Regarding the meteorological stations across the urban area, some differences were also observed between the acquired values of both air temperature and relative humidity. In Figure 6a,b, the areas are divided into areas where the NDVI index exceeds 0.3 units (higher vegetation density) and those where the NDVI index is below 0.3 units (lower vegetation density), and the box plots illustrate the minimum, first-quartile, median, third-quartile and maximum values of air temperature and relative humidity. Higher values of air temperature (0.5 °C in the case of total average and 0.46 °C in the case of median value) and lower values of relative humidity (0.8% in case of total average and 0.9% in case of median value) appeared when the NDVI index is lower than 0.3 units, indicating in that way the importance of vegetation parts in the urban environment.

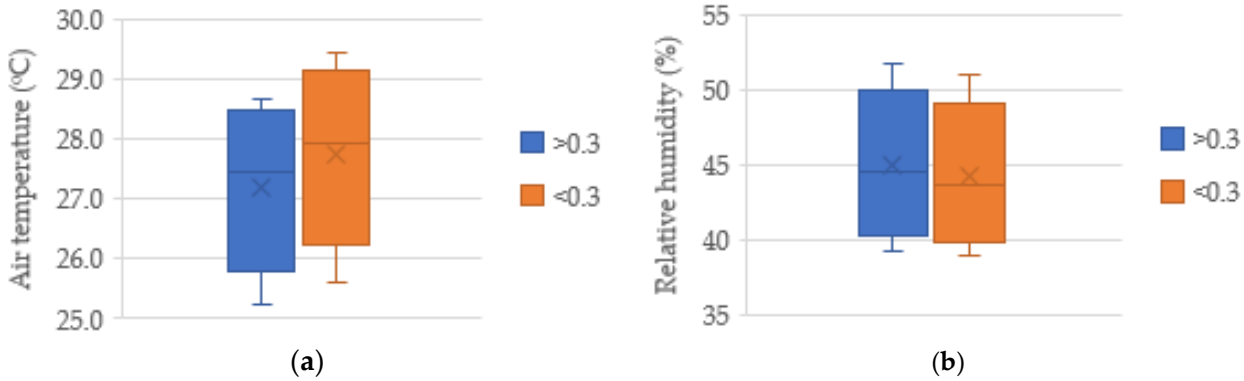

(**a**) (**b**)

Figure 6. (**a**) Air temperature and (**b**) Relative humidity distribution in relation to the NVDI index of meteorological stations' location areas.

3.3. Remote Sensing

3.3.1. Landsat8 Albedo

The albedo is an important parameter that affects climate [54]. Table 7 presents the different materials' cover area, both in m^2 and percentage (%) (as designed and calculated in the QGIS environment), as well as the albedo values derived from both the literature review [55–57] and from the Landsat satellite sensor (Equation (18)). As can be noticed, the total average albedo value derived from the Landsat8 sensor was found to be quite close with that obtained from the literature review. However, the analysis that concerns individual surface cover materials revealed some inaccuracies between these two values. This may be attributed to the spatial resolution of the Landsat8 sensor. Landsat8 offers spectral images with a spatial resolution of 30 m. For this reason, some surfaces cannot be accurately identified because they are affected by neighbor types of surfaces (neighbor pixels). What can be concluded, though, is that there is a large area of conventional concrete materials with medium to low values of solar reflectivity that cause high surface temperature values, as can be seen in Table 4.

Table 7. Albedo coefficient of the different cover materials in the study area.

Material Type	Cover Area (M^2)	Cover Area (%)	Albedo (Literature)	Cover Area (%) × Albedo	Albedo (Landsat8)
Pavement tile	4917.80	0.26	0.20 [a]	0.05	0.22
Sand	2187.50	0.12	0.58 [b]	0.07	0.27
Grass	6778.80	0.36	0.29 [c]	0.11	0.27
Rubber	515.4	0.03	0.34 [b]	0.01	0.28
Concrete	969.9	0.05	0.34 [c]	0.02	0.26
Granite	3296.40	0.18	0.26 [b]	0.05	0.26
Average	18,665.90	1	-	0.3	0.26

[a] [55], [b] [56], [c] [57].

3.3.2. Downscaled Satellite Images and Field Measurements

As has already been mentioned, 24 MODIS satellite images were collected and used in a downscaling technique. Figure 7a,b presents the linear correlation between the downscaled and measured values of surface temperature. The total average values that were derived from the TC (33.7 °C) and IR (33.9 °C)) instruments were found to be quite close each other, and both of them were quite close to the ones derived from the downscaling method (34.0 °C).

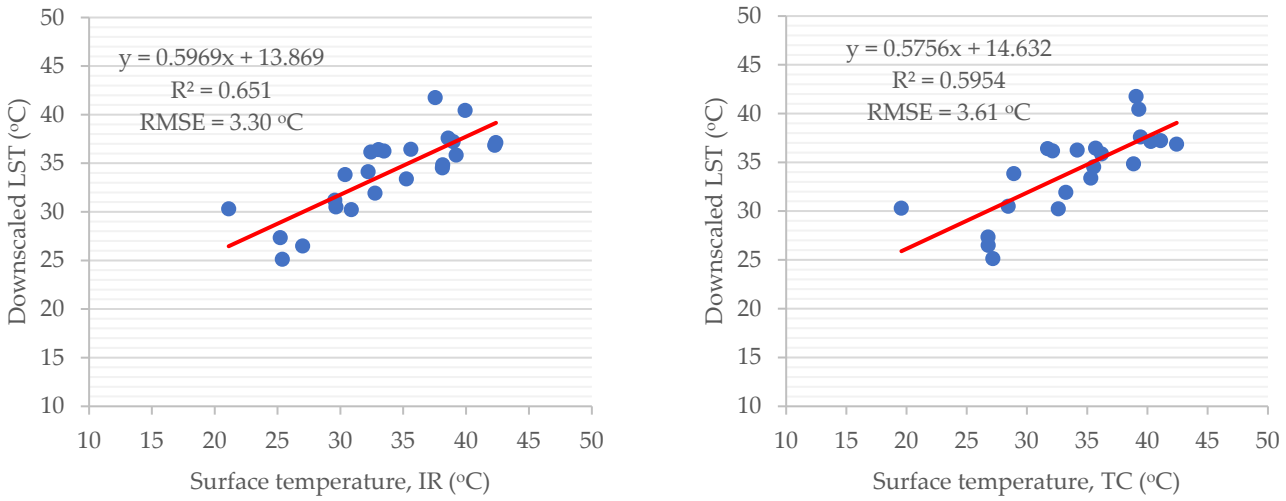

(**a**) (**b**)

Figure 7. Linear correlation between: (**a**) downscaled and IR-measured surface temperature values; (**b**) downscaled and TC-measured surface temperature values.

Concerning the correlation between the observed and remote sensing data, no great differences between the IR and TC instruments were observed. More precisely, the RMSE index between the IR and downscaled surface temperature was found to be equal to 3.30 °C and the coefficient of determination, $R^2 = 0.65$. The correlation between surface temperature derived from the IR instrument and downscaled satellite images is described as follows:

$$y = 0.60 \cdot x + 13.87, R^2 = 0.65 \quad (21)$$

where

- y is the surface temperature derived from satellite images;
- x is the surface temperature derived from sensors.

On the other hand, the RMSE value between the TC and downscaled surface temperature values was 3.61 °C and the $R^2 = 0.60$. The correlation between surface temperature derived from the thermal camera and the downscaled satellite images is described as follows:

$$y = 0.58 \cdot x + 14.63, R^2 = 0.60 \quad (22)$$

Figure 8a–e presents the quartile analysis between the downscaled surface temperature values and those derived from measurement instruments for the different types of surface material areas. As can be seen, in the case of pavement areas, the estimated values were found to approach the average values derived from measurement instruments. More precisely, the estimated median value derived from the downscaled LST was found to be equal to 35.2 °C and the median value derived from IR, found to be equal to 36.8 °C. The accordance value of the TC was found to be equal to 35.2 °C. Concerning the total average, the estimated average value was found to be equal to 34.8 °C, 0.9 °C lower than that derived from the IR and 0.3 °C lower than that derived from the TC instrument. On the other hand, in the area that is covered with rubber material, larger errors between estimated values and measurements appeared. More precisely, the median value concerning the downscaled data was found to be equal to 36.0 °C, which means that it was 16.7 °C lower than that acquired from the IR instrument and 17.6 °C lower than that derived from the TC. The average value derived from the downscale method in rubber areas appeared to be 16.5 °C lower than the ones derived from both the IR and TC instruments.

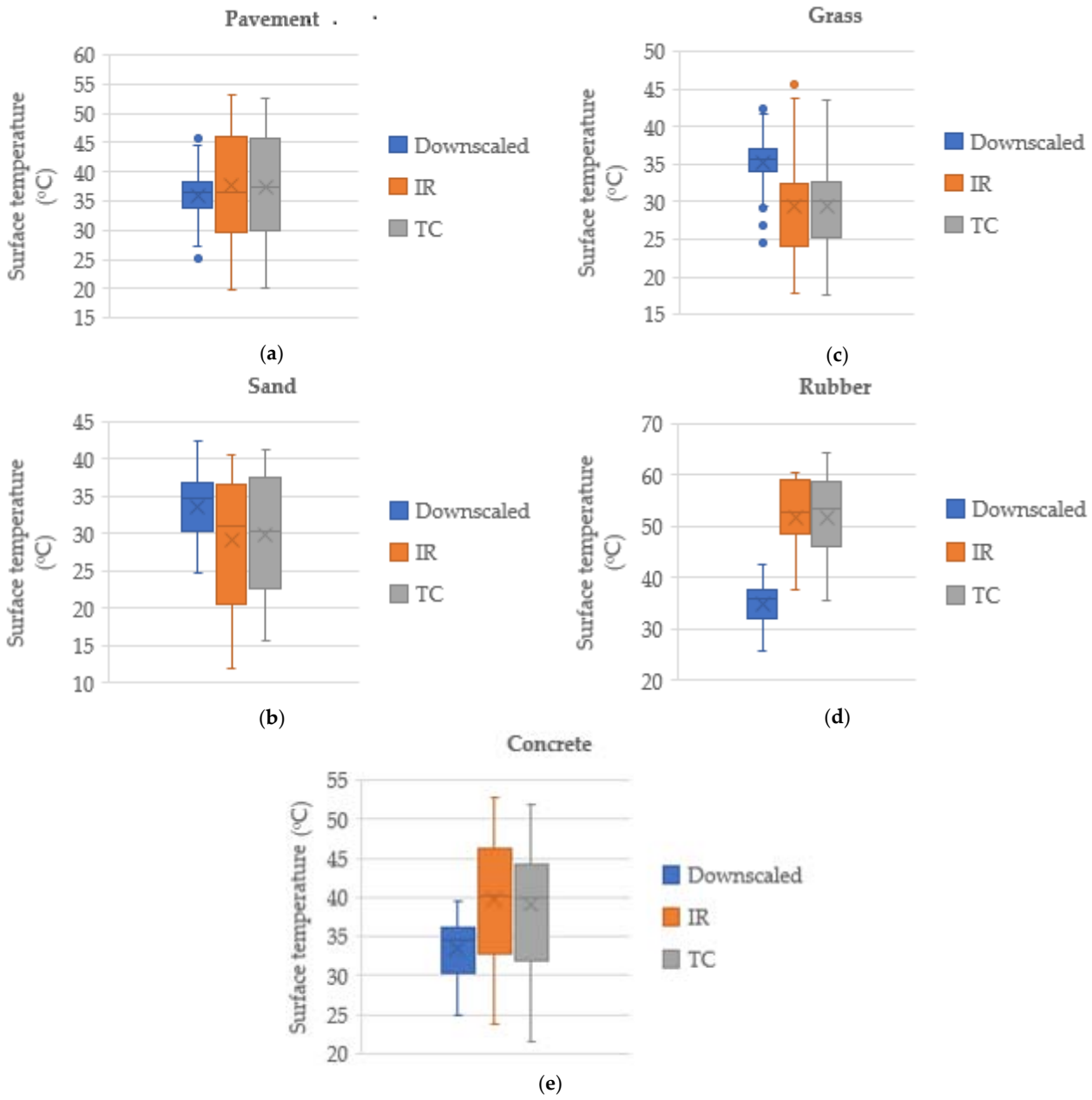

Figure 8. Investigation of the downscaled LST values in different material surface areas: (**a**) pavement tile; (**b**) sand; (**c**) grass; (**d**) rubber; (**e**) concrete.

An investigation of the downscaled LST values in relation to sun exposure and albedo coefficient took place, which is presented in Figure 9a,b. The areas are divided into those exposed to solar radiation and those that were shaded (Figure 9a) and into areas where the albedo coefficient exceeds 0.3 units and into areas where the value is below 0.3 (Figure 9b). Concerning sun exposure, the total average value in shaded places was found to be warmer up to 1.1 °C than those exposed to solar radiation, indicating in that way that the downscaling procedure was not able to detect the shading, and then non-shading, effects at specific points in a microscale region. On the other hand, as far as concerns albedo effects, the average downscaled LST value was found to be 1.3 °C higher in areas where the albedo coefficient was below 0.3 units. Differences appeared also in the case of the median value, as the areas with low albedo were found to be 0.9 °C warmer compared to areas with a higher albedo coefficient. It can be concluded from the results that the surface temperature values that were derived from the downscaling methods can describe with accuracy the

actual ones. However, in the current study, there are surfaces that cover a small portion of the total selected area (in terms of m^2) and for this reason the estimated surface temperature values cannot be described with accuracy in those surfaces due to the low spatial resolution that the satellite data offer. Inaccuracies of downscaled LST results were observed over grass areas as well. These inaccuracies could be attributed to the fact that the surface temperature measuring point is quite unstable in grass areas, and different values inside a few square meters can be detected. These fluctuations of the surface temperature are reflected in the estimated downscaled LST values.

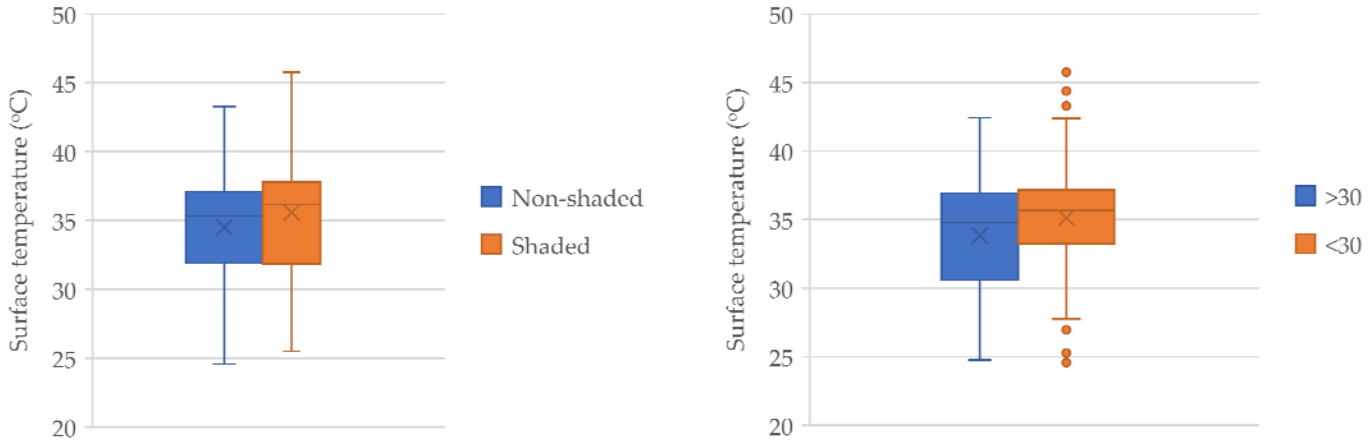

Figure 9. Investigation of the downscaled LST values in relation to (**a**) sun exposure; (**b**) albedo coefficient.

3.3.3. Landsat8 Split-Window LST Algorithms Assessment

Several split-window (SW) algorithms that are widely applied to the Landsat8 sensor were assessed, and the most appropriate one, in terms of overall performance, will be further adopted in the current study to examine the derived LST parameter in relation to sun exposure and albedo coefficient. The algorithms were presented in Section 2.5, Equations (1), (7), (8) and Equations (12)–(17) in Table 3. In total, six Landsat8 datasets were available during the measurement period, as can be seen in Table 1. Table 8 shows the overall performance of the split-window algorithms. As can be seen, some errors appeared in most split-window algorithms concerning the overall performance, as the RMSE index was found to exceed 2 °C in all cases.

Table 8. The performance of numerous split-window algorithms in terms of RMSE values compared to both IR and TC instruments.

Algorithm	RMSE, IR (°C)	RMSE, TC (°C)
Meng, Enterprise [a]	6.44	5.86
Meng, Wan [a]	3.52	3.99
Du, Wan [b]	2.23	2.17
Gerace, Wan [c]	2.93	2.5
Meng, Jimenez [a]	2.79	2.47
Jimenez-Munoz [d]	2.33	2.09
Coll & Caselles [e]	33.89	34.42
Kerr [f]	2.46	2.26
McClain [g]	6.91	7. 53
Price [h]	4.72	4.33
Sobrino [i]	3.88	3.62
Ulivieri [j]	3.9	3.5

[a] [45], [b] [46], [c] [47], [d] [29], [e] [48], [f] [49], [g] [50], [h] [51], [i] [52], [j] [53].

Generally, there are several factors that affect the performance of split-window algorithms. Firstly, there is the spatial resolution of the Landsat8 product (30 m) [13,14]. Especially, as far as concerns a small urban area like the current study area, the low spatial resolution may affect the final results. Secondly, the measurement procedure may be another factor. Measuring the surface temperature of different materials distributed along a study area is not an easy task, and in the current study, measurements were taken by moving from one measurement point to another (approximately 5 min was required for measurement at each point). So, some surface temperature values extracted from in situ measurements did not coincide with those extracted from satellite images. Thirdly, the spectral emissivity (band 10 and band 11) is another reason that may affect the results derived from split-window algorithms, as has already been mentioned in previous studies [49]. Finally, water vapor content may also affect the final results of some algorithms. More specifically, in previous studies, a slightly deterioration in the performance of split-window algorithms was detected by increasing the water vapor content [45].

In the current study, the water vapor content values (MSWCVR) calculated from Equation (9) varied from 3.56 g cm^{-2} to 5.55 g cm^{-2}. Taking into consideration that the values remained above 3.5 g cm^{-2} during the measurement campaign, high levels of water vapor content may be another reason that discrepancies were observed between measurement values of the surface temperature and those derived from split-window algorithms. However, the most appropriate one was found to be the 'Generalized split-window algorithm' from Wan and Dozier, 1996 (Equation (7)) [42], and elaborated by Du et al., 2015, and therefore referred to as the 'Du, Wan algorithm' [46]. The coefficients C_i ($i = 0 \sim 7$) of the 'Du, Wan algorithm', can be found in Table 2, column 3 [46]. The RMSE value of the algorithm was found to be equal to 2.23 °C in the IR case and 2.17 °C in the TC case. Figure 10a,b present the correlation between the land surface temperature (LST) derived from the 'Du, Wan algorithm' [46] and the surface temperature derived from the measurement instrument. More specifically, the equation that describes the correlation between the surface temperature derived from the IR instrument and that derived from 'Du, Wan algorithm' is presented as follows:

$$y = 1.02 \cdot x + 0.41, R^2 = 0.83 \quad (23)$$

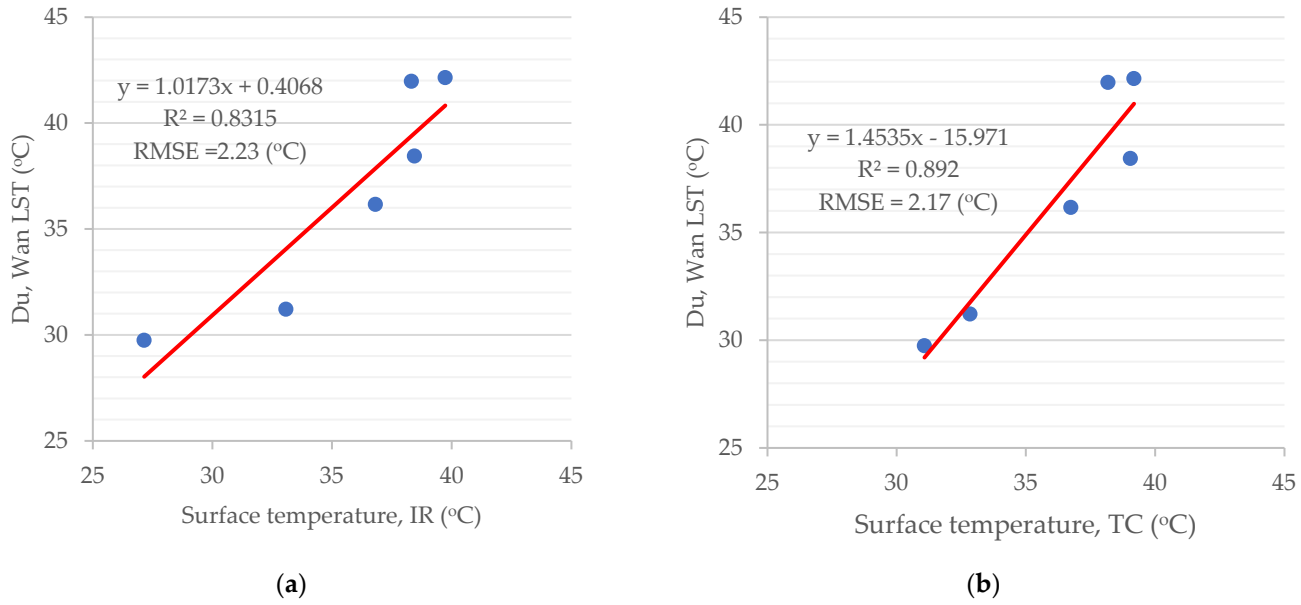

(**a**) (**b**)

Figure 10. Correlation between land surface temperature derived from the 'Du, Wan algorithm' and surface temperature acquired from: (**a**) IR instrument; (**b**) TC instrument.

On the other hand, the equation that describes the correlation between the surface temperature derived from the TC instrument and that derived from the 'Du, Wan algorithm is presented as follows:

$$y = 1.45 \cdot x - 15.97, R^2 = 0.89 \quad (24)$$

It can be concluded that the RMSE index is in line with that appearing in Figure 7a,b. However, in both Figure 10a,b, the R^2 was found to be 0.83 in the case of the IR and 0.89 in the case of the TC (strong correlation in both cases). It has to be taken into consideration, though, that only 6 Landsat8 satellite images were available during the measurement period due to cloud effects. Concerning the performance of the other algorithms, close results to those observed from the 'Du, Wan algorithm' appeared in the case of the algorithm proposed from Jimenez-Munoz (Equation (8)) (the coefficients C_i ($i = 0 \sim 5$) can be seen in Table 2, column 6) [29]. In more detail, the RMSE index between the estimated LST values from derived from the 'Du, Wan algorithm' and those derived from the IR instrument were found to be equal to 2.33 °C. On the other hand, the RMSE index between the estimated LST values from the 'Du, Wan algorithm' and those derived from the IR instrument were found to be equal to 2.09 °C. Large errors appeared in the case of the 'Coll&Caselles algorithm' (Equation (12)) [48]. Those errors, though, could be attributed to the fact that the referenced algorithm has been developed in arid and semi-arid climates. Taking that into consideration, the referenced algorithm is not able to calculate an LST parameter in the urban area of Milan. What can be concluded from Table 8, is that some forms of the generalized split-window algorithm and some forms of the Jimenez-Munoz algorithm showed a better performance than the rest that were included in the current study.

Among all selected algorithms, the 'Du, Wan algorithm' has shown the best applicability in terms of the RMSE index, and therefore it was selected for further analysis. In Figure 11a–e, the quartile analysis between the LST values derived from the 'Du, Wan algorithm' and the surface temperature derived from measurement instruments on all types of material surface areas is presented. As can be seen, when even a small sample is available, the results are in line with those derived from the downscaling method and presented in Figure 8a–e. An investigation of the LST values derived from the 'Du, Wan algorithm' in relation to sun exposure and albedo coefficient also took place, and the results are presented in Figure 12a,b. In the first case, the calculation of the LST directly from channels 10 and 11 of the Landsat8 sensor appeared to be more accurate, contrary to what is presented in Figure 9a, as differences can be detected between first-quartile and median values. More specifically, in the first quartile, the value that derived from the non-shaded areas was found to be 1.77 °C warmer than that from the areas that were shaded. Also, the median value of non-shaded areas was found to be 0.31 °C warmer as well. Also, the average value of shaded areas was found to be equal to that observed in non-shaded areas (37.1 °C). Concerning albedo analysis, the average LST value was found to be 2.2 °C higher in areas where the albedo coefficient is below 0.3 units, showing in that way similar results to those presented in Figure 8b. What can be concluded from the results is that shading parts in a microscale area can be detected more accurately using split-window algorithms instead of downscaling techniques.

3.3.4. Landsat8 Split-Window (SW) LST Algorithms Analysis per Surface Area

The performance of the split-window algorithms presented in Table 8 was assessed for each material surface area in the study area. Figure 13a–e presents, for each material, the RMSE index between the surface temperature values (LST) derived from different split-window algorithms and those measured from both measurement instruments (mean value of IR and TC). As it can be seen, in sand areas the algorithms that in the current study is referred as 'Meng, Wan algorithm' appeared to be the most accurate one, as the RMSE index was equal to 3.64 °C. This algorithm is the 'Generalized split-window algorithm' from Wan and Dozier, 1996 (Equation (7)) [42], and therefore elaborated by Meng et al., 2019 [45]. The referenced values C_i ($i = 0 \sim 7$) are presented in Table 2, column 2 [45]. Accordingly, in grass areas, the 'McClain algorithm' (Equation (14)) [50] showed the most

representative values, as the RMSE index was found to be equal to 2.27 °C. On the other hand, in pavement tile areas, the 'Generalized split-window algorithm' called the 'Du, Wan algorithm' (Equation (7)) appeared to be the most accurate one, as the RMSE index was found to be equal to 3.06 °C. Finally, in both concrete and rubber areas, the 'Enterprise algorithm' (Equation (1)) [35,36], called the 'Meng, Enterprise algorithm' in the current study, with the referenced values C_i ($i = 0 \sim 5$) presented in Table 2, column 1 [45], showed the best applicability as the RMSE index was found to be equal to 2.94 °C and 12.77, respectively.

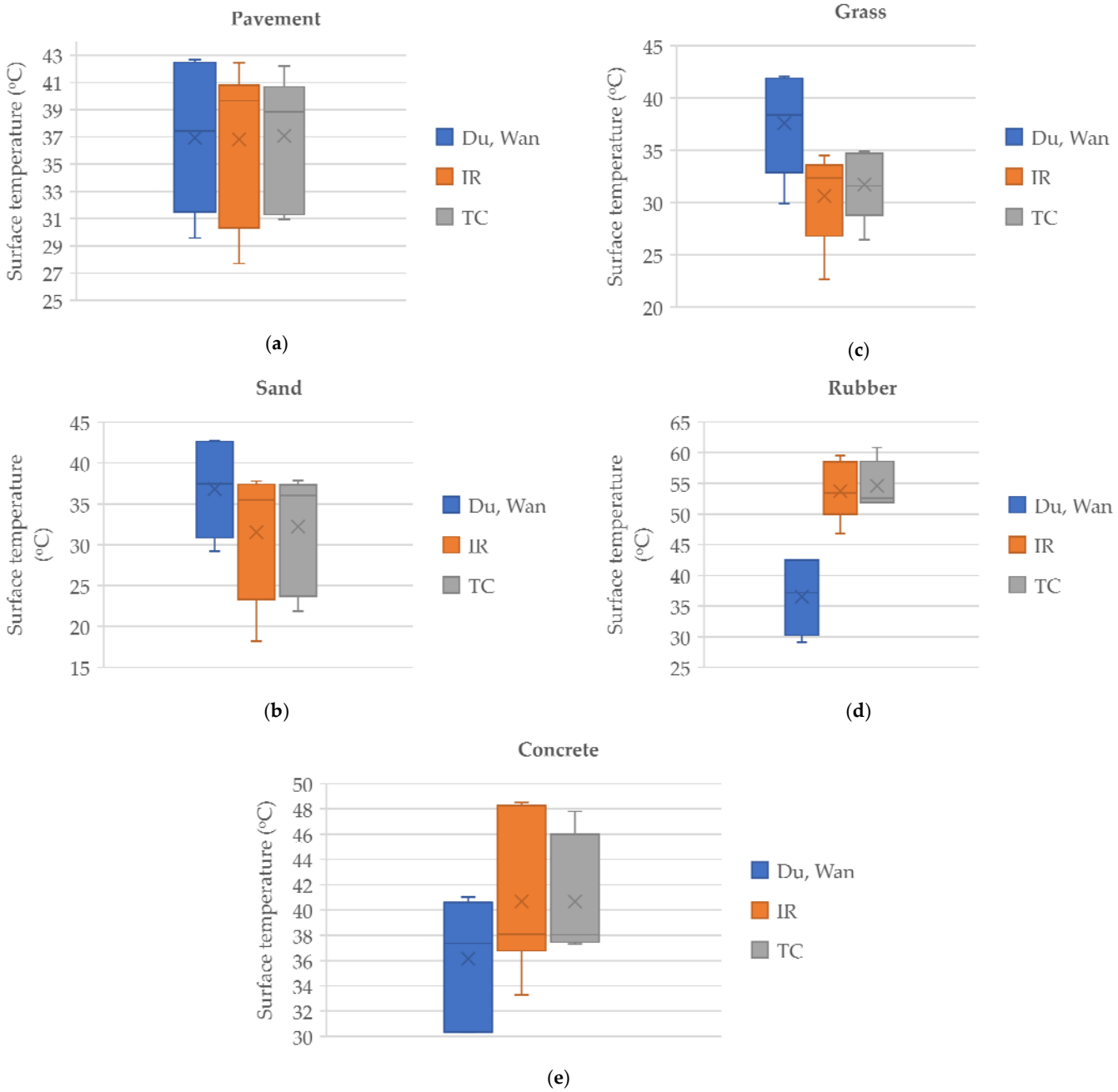

Figure 11. Investigation of the LST values with different materials: (**a**) pavement tiles; (**b**) sand; (**c**) grass; (**d**) rubber; (**e**) concrete.

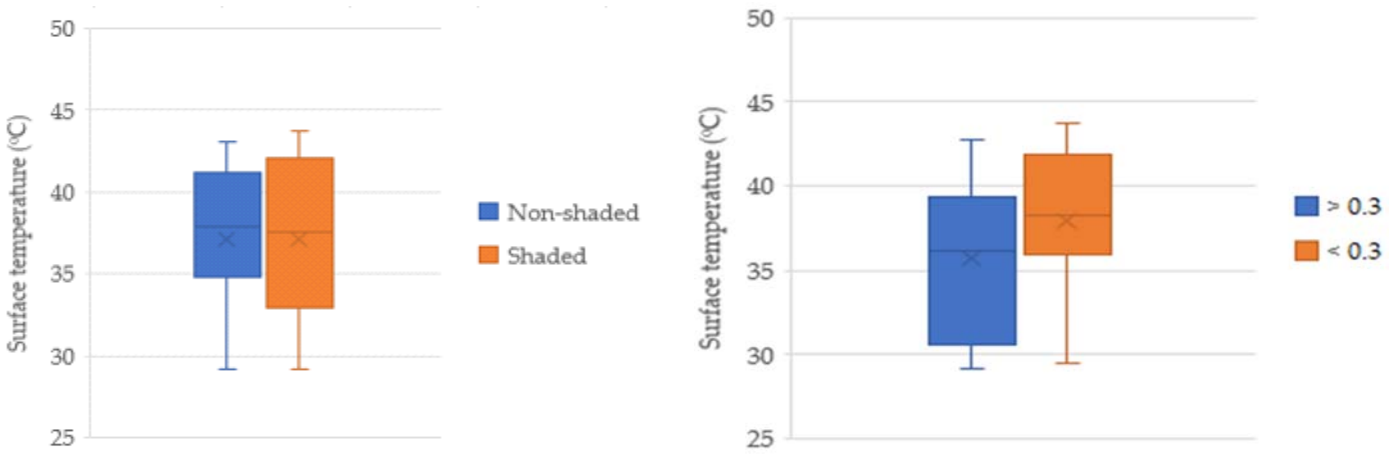

Figure 12. Investigation of the LST values in relation to (**a**) sun exposure; (**b**) albedo coefficient.

A combination of the four 'split-window algorithms' with a low RMSE index for each material, as a tool to detect the surface temperature inside an urban environment, was applied. In more detail, in pavement areas, the 'Du, Wan algorithm' was applied. In sand areas, the 'Meng, Wan algorithm' was applied. Accordingly, in grass areas, the 'McClain algorithm' and finally, in both rubber and concrete areas, the 'Meng, Enterprise algorithm' were applied. Figure 14a,b presents the correlation between the land surface temperature (LST) derived from the combined split-window algorithms (referred to as Combined SW) and the surface temperature acquired from both measurement instruments. As can be seen, the RMSE index was found to be 1.64 °C concerning the comparison of the LST derived from the combination of SW algorithms and the values derived from IR instrument, and 2.22 (°C) in the case of the TC instrument. Comparing the results with those presented in Figure 10a,b, it can be concluded that there is an average reduction of 0.27 °C of the RMSE index. Figure 15a–e presents the spatial distribution of surface temperature as derived from the combined 'split-window algorithms' for the different surface areas.

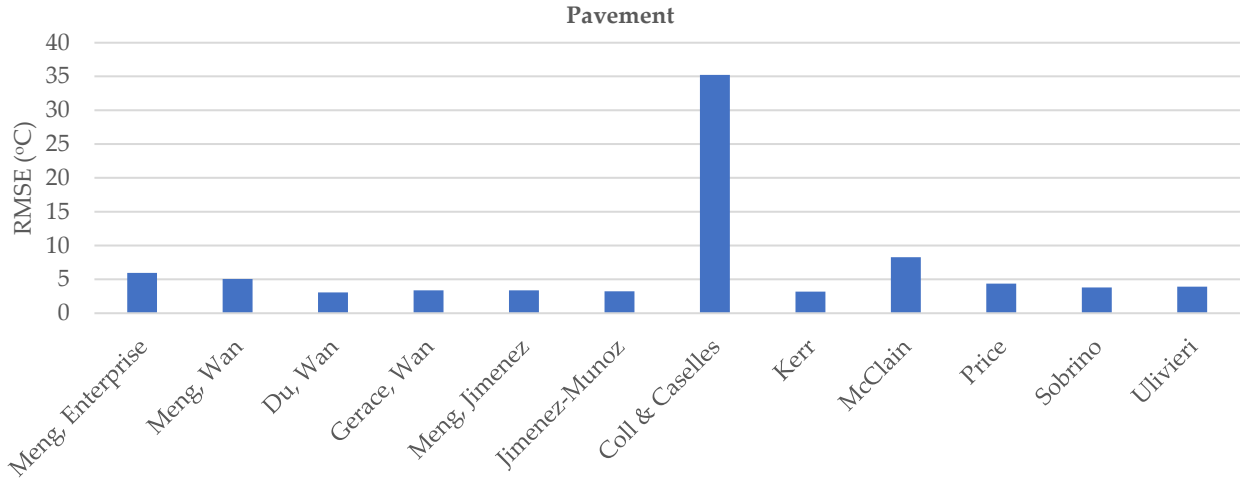

Figure 13. *Cont.*

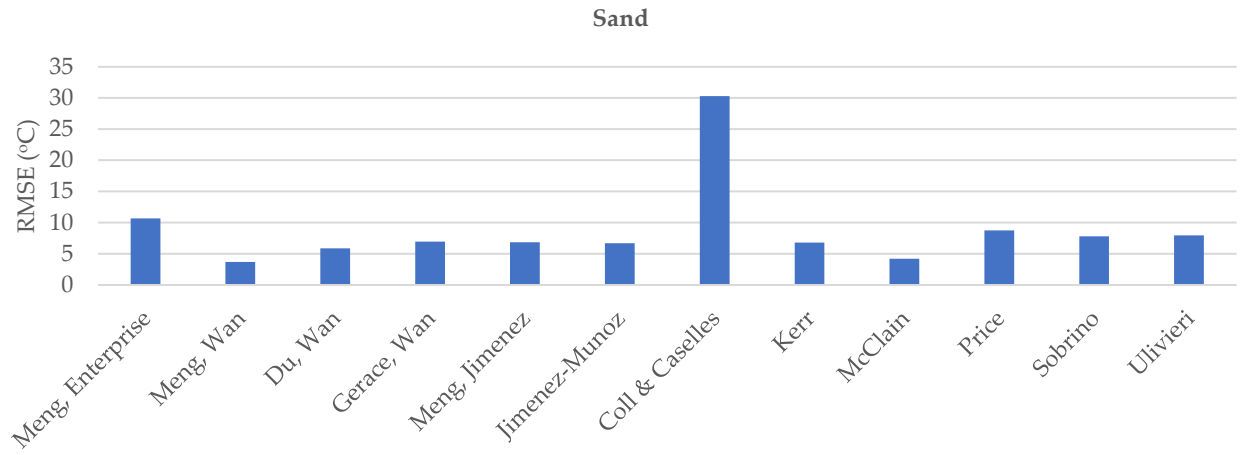

(**b**)

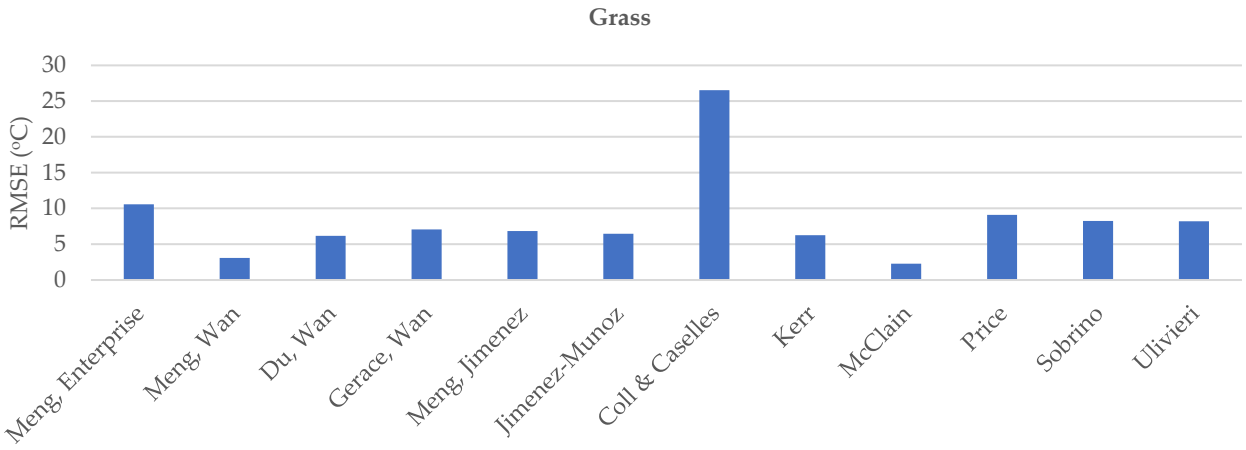

(**c**)

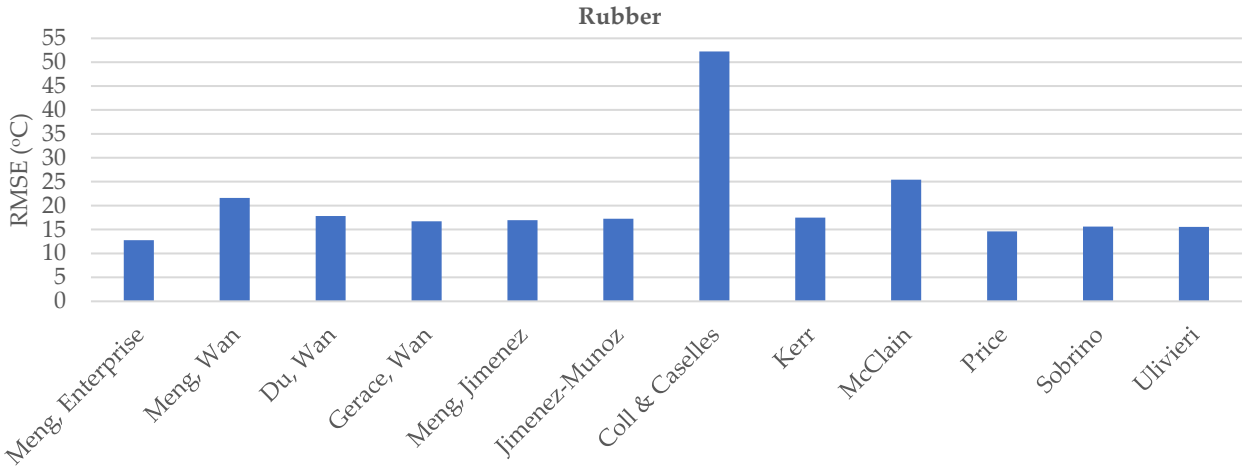

(**d**)

Figure 13. *Cont.*

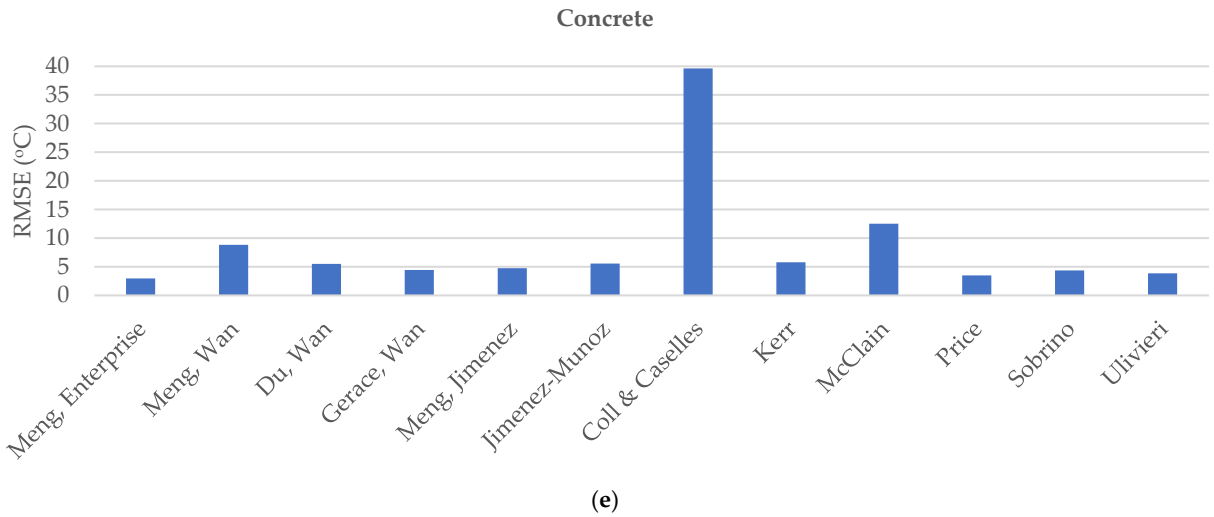

Figure 13. Root mean square error index (RMSE) for the applied split-window algorithms concerning (**a**) pavement tile areas; (**b**) sand areas; (**c**) grass areas; (**d**) rubber areas; (**e**) concrete areas.

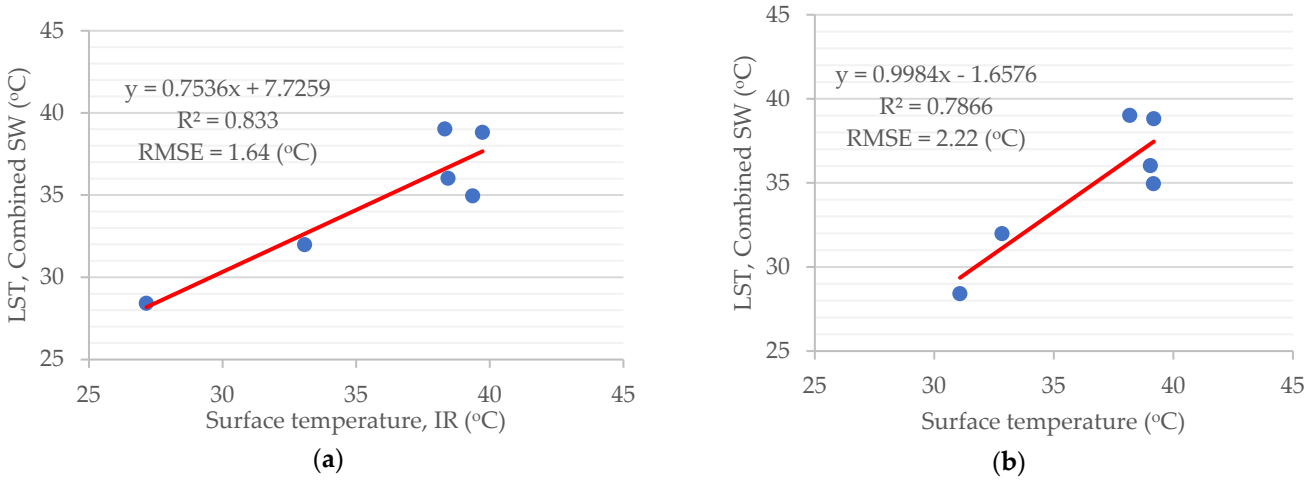

Figure 14. (**a**) Correlation between land surface temperature derived from the combined split-window algorithms and surface temperature acquired from: (**a**) IR instrument (**b**) TC instrument.

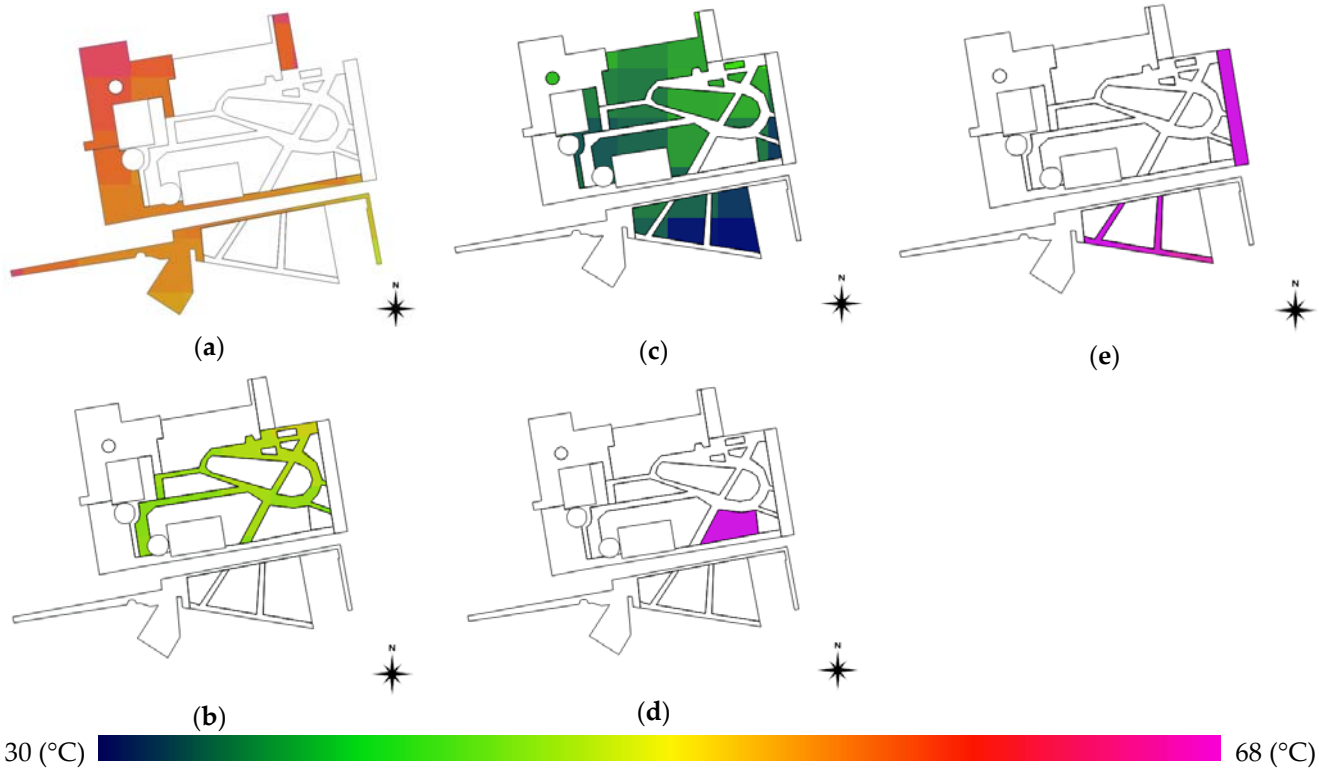

Figure 15. Spatial distribution of surface temperature as derived from combined split-window algorithms in: (**a**) grass areas; (**b**) sand areas; (**c**) pavement areas; (**d**) concrete areas; (**e**) rubber areas.

4. Discussion

The field measurements that were conducted in the Bosco Verticale area in the city of Milan showed that conventional materials produce high levels of surface temperature. However, the analysis of shaded and non-shaded areas showed a significant reduction in both surface and air temperature values, indicating in that way the importance of the presence of shading parts in urban areas during the spring and summer periods. The elements that offer shading over the Bosco Verticale areas are mainly tall buildings and trees. In contrast, the surface temperature reduces significantly in the natural surfaces that cover the rest of the area.

The comparison of the data collected in the study area with those derived from fixed weather stations showed differences, as the study area was found to be significantly warmer in terms of air temperature, indicating that a more detailed study is needed. Comparing the data of the fixed weather stations, the regions with low NDVI levels were found to be warmer in comparison to those with high levels of NDVI index. The adaption of the TsHARP downscaling technique showed relatively accurate results concerning the comparison between the average estimated and measured values. The analysis of the downscaled values derived from different surface areas showed that, in pavement tile areas, the TsHARP method is relatively accurate. Also, the downscaled values were found to be warmer in areas with low surface reflectance (albedo). On the other hand, the sunny places of the study area were found to be cooler when they were compared with those that were shaded.

Application of several 'split-window algorithms' showed that some forms of the 'Generalized split-window algorithm' and some forms of the 'Jimenez-Munoz algorithm' showed a better performance in comparison to the rest that were included in the current study. The algorithm that, in the current study, is called the 'Du, Wan algorithm' showed the best applicability in terms of the RMSE index (2.23 °C in case of IR and 2.17 °C in case of TC). The analysis of the 'Du, Wan algorithm' per surface area showed relevant results to

those derived from the downscaled LST, as the 'Du, Wan algorithm' was found to be more precise in pavement tile areas.

Concerning the albedo analysis, the 'Du, Wan algorithm' showed that the areas with relatively low albedo were found to be 2.2 °C warmer. Also, the LST parameter that derived from the 'Du, Wan algorithm' was found to be slightly affected from shading parameters, despite the fact that no differences were detected in the total average values of shaded and non-shaded areas. More specifically, the first-quartile value of shaded areas was found to be 1.27 °C lower than that derived from non-shaded areas, and the according median value was found to be 0.31 °C lower as well. Concerning the performance of the selected 'split window algorithms' per surface area, the results revealed that, in sand areas, the 'Meng, Wan algorithm' showed the best applicability. Accordingly, in grass areas, more accurate results were observed from the 'McClain algorithm'; in the case of pavement tile surfaces, the 'Du, Wan algorithm' showed the best applicability; and finally, in both rubber and concrete areas, the results derived from the 'Meng, Enterprise algorithm' were found to be the most reliable among all the included 'split-window algorithms'. An application of these four algorithms to a single model was found to reduce the RMSE index up to 1.64 °C in the case of the IR instrument and 2.22 °C in the case of the TC.

5. Conclusions

In the current study, an open area inside a large urban environment was investigated. Firstly, different methodology approaches have been selected to assess the microclimatic parameters inside the urban area. A measurement campaign took place to monitor the values of air temperature, surface temperature and relative humidity in the study area. Also, six meteorological stations inside the city of Milan were selected and the monitored meteorological parameters were compared with those collected from in situ measurements. Finally, simultaneous remote sensing data were also collected and the extracted LST parameter compared with the values experimentally gathered, in order for downscaling techniques and the application of several split-window algorithms to be assessed.

The comparison between the meteorological values that were experimentally measured with the ones gathered from nearby stations revealed great deviations. These differences may be attributed to the different measurement heights, as the measurement campaign in the 'Bosco Verticale area' took place at a height of 1.5 m above ground and therefore was vulnerable to the extremely high levels of surface temperature that is produced when solar radiation is at its peak. On the other hand, the meteorological stations are placed at a higher height, and therefore the differences between the areas may be exaggerated in terms of microclimatic conditions. However, further investigation should take place in order for the differences between the 'Bosco Verticale' and the rest of the areas to be examined more precisely. Concerning the areas where fixed meteorological stations area were placed, both the Zavattari and Lambrate areas appeared to have high average air temperature values. Both areas are located far from the center of the urban area of Milan and both areas are not considered as densely built areas. The relatively high air temperature values may be attributed to the fact that these areas during daytime are not shaded sufficiently, and many parts of these areas are exposed to solar radiation. This may lead to high temperature values during daytime. Another factor that may lead to great differences between meteorological stations areas is that of vegetation. In order for the vegetation parameter to be assessed, the NDVI index was used. The NDVI index that was derived remotely showed that the areas where the index exceeded 0.30 units appeared to have lower values compared to those where the NDVI index was below 0.30 units in terms of air temperature, showing in that way the necessity of the greenery inside urban environments.

The field measurements showed that the areas that are covered with conventional artificial materials are warmer than those covered with natural ones. The shading elements (both greenery and tall buildings) offer low values of both surface and air temperature. The addition of materials with high solar reflectivity may be an effective solution in non-shaded

areas. Concerning remote sensing methods, downscaling techniques showed relatively satisfactory results. However, some areas still remained unidentified for the accurate calculation of the LST parameter, even when the sharpening method was employed at a microscale level (the rubber areas in the current study are the most representative example). This may be attributed to the low spatial resolution of the remote sensing data that are freely available [13,14,23,31]. Also, the shaded and non-shaded areas are not detected with the application of downscaling techniques.

Finally, the assessment of different Landsat8 split-window algorithms, in terms of overall performance, showed that some forms of the 'Generalized split-window algorithm' and some forms of the 'Jimenez-Munoz algorithm' showed better performance in comparison to the rest that were included in the current study. An analysis of the performance of the applied split-window algorithms per different material surface area showed that a combination of different algorithms inside the urban area reduces errors in terms of the RMSE index. In future studies, more assessments of remote sensing techniques need to be performed inside urban environments at microscale levels in order to determine the parameters that increase the accuracy of remote sensing methods in an urban complex environment.

Author Contributions: Conceptualization, G.K. and A.D.; Methodology, G.K. and A.D.; Validation, G.K.; Investigation, G.K., J.T. and A.D.; Resources, J.T.; Data curation, G.K.; Writing—original draft, G.K. and A.D.; Writing—review & editing, A.D.; Supervision, J.T. and A.D. All authors have read and agreed to the published version of the manuscript.

Funding: This research received no external funding.

Institutional Review Board Statement: Not applicable.

Informed Consent Statement: Not applicable.

Data Availability Statement: Data is contained within the article.

Acknowledgments: It should be acknowledged that the current monitoring survey in Milan city was carried out with a grant of the DUTH ERASMUS + Program obtained by Kalogeropoulos G. Also, the accomplishment of the current study was co-financed from Greece and the European Union (European Social Fund) through the Operating Program 'Development of Human Resources through the implementation of doctoral thesis Action 2: Program for granting IKY scholarships to candidates from Greece.' Finally, we would like to thank Gianelle Vorne, ARPA Lombardia, for providing the climatic data of the fixed meteorological stations that were used in the current study.

Conflicts of Interest: The authors declare no conflict of interest.

References

1. Mohsin, T.; Gough, W.A. Characterization and estimation of urban heat island at Toronto: Impact of the choice of rural sites. *Theor. Appl. Clim.* **2012**, *108*, 105–117. [CrossRef]
2. Jin, M.S. Developing an Index to Measure Urban Heat Island Effect Using Satellite Land Skin Temperature and Land Cover Observations. *J. Clim.* **2012**, *25*, 6193–6201. [CrossRef]
3. Oke, T.R. City size and the urban heat island. *Atmos. Environ.* **1973**, *7*, 769–779. [CrossRef]
4. Oke, T.R.; Mills, G.; Christen, A.; Voogt, J. *Urban Climates*; Cambridge University Press: Cambridge, UK, 2017.
5. Bottyán, Z.; Kircsi, A.; Szegedi, S.; Unger, J. The relationship between built-up areas and the spatial development of the mean maximum urban heat island in Debrecen, Hungary. *Int. J. Clim.* **2005**, *25*, 405–418. [CrossRef]
6. Bottyán, Z.; Unger, J. A multiple linear statistical model for estimating the mean maximum urban heat island. *Theor. Appl. Climatol.* **2003**, *75*, 233–243. [CrossRef]
7. Dimoudi, A.; Zoras, S.; Kantzioura, A.; Stogiannou, X.; Kosmopoulos, P.; Pallas, C. Use of cool materials and other bioclimatic interventions in outdoor places in order to mitigate the urban heat island in a medium size city in Greece. *Sustain. Cities Soc.* **2014**, *13*, 89–96. [CrossRef]
8. Pichierri, M.; Bonafoni, S.; Biondi, R. Satellite air temperature estimation for monitoring the canopy layer heat island of Milan. *Remote Sens. Environ.* **2012**, *127*, 130–138. [CrossRef]
9. Pongrácz, R.; Bartholy, J.; Dezső, Z. Application of remotely sensed thermal information to urban climatology of Central European cities. *Phys. Chem. Earth Parts A/B/C* **2010**, *35*, 95–99. [CrossRef]

10. Weng, Q. Thermal infrared remote sensing for urban climate and environmental studies: Methods, applications, and trends. *ISPRS J. Photogramm. Remote Sens.* **2009**, *64*, 335–344. [CrossRef]
11. Chapin, F.S.; Iii, F.S.C.; Sturm, M.; Serreze, M.C.; McFadden, J.P.; Key, J.R.; Lloyd, A.H.; McGuire, A.D.; Rupp, T.S.; Lynch, A.H.; et al. Role of Land-Surface Changes in Arctic Summer Warming. *Science* **2005**, *310*, 657–660. [CrossRef]
12. Kalnay, E.; Cai, M. Impact of Urbanization and Land-Use Change on Climate. *Nature* **2003**, *423*, 528–531, Erratum in *Nature* **2003**, *425*, 102. [CrossRef]
13. Aniello, C.; Morgan, K.; Busbey, A.; Newland, L. Mapping micro-urban heat islands using LANDSAT TM and a GIS. *Comput. Geosci.* **1995**, *21*, 965–967, 969. [CrossRef]
14. Liu, L.; Zhang, Y. Urban Heat Island Analysis Using the Landsat TM Data and ASTER Data: A Case Study in Hong Kong. *Remote Sens.* **2011**, *3*, 1535–1552. [CrossRef]
15. Mhawej, M.; Abunnasr, Y. Daily Ten-ST-GEE: An open access and fully automated 10-m LST downscaling system. *Comput. Geosci.* **2022**, *168*, 105220. [CrossRef]
16. Guzinski, R.; Nieto, H.; Sánchez, R.R.; Sánchez, J.M.; Jomaa, I.; Zitouna-Chebbi, R.; Roupsard, O.; López-Urrea, R. Improving field-scale crop actual evapotranspiration monitoring with Sentinel-3, Sentinel-2, and Landsat data fusion. *Int. J. Appl. Earth Obs. Geoinf.* **2023**, *125*, 103587. [CrossRef]
17. Cai, G.; Du, M.; Xue, Y. Monitoring of urban heat island effect in Beijing combining ASTER and TM data. *Int. J. Remote Sens.* **2011**, *32*, 1213–1232. [CrossRef]
18. Cheval, S.; Dumitrescu, A. The July urban heat island of Bucharest as derived from modis images. *Theor. Appl. Clim.* **2009**, *96*, 145–153. [CrossRef]
19. Gallo, K.P.; McNab, A.L.; Karl, T.R.; Brown, J.F.; Hood, J.J.; Tarpley, J.D. The use of NOAA AVHRR data for assessment of the urban heat island effect. *J. Appl. Meteorol.* **1993**, *32*, 899–908. [CrossRef]
20. Orlanski, I. A Rational Subdivision of Scales for Atmospheric Processes. *Bull. Am. Meteorol. Soc.* **1975**, *56*, 527–530.
21. Sicignano, E.; Di Ruocco, G.; Melella, R. Mitigation Strategies for Reduction of Embodied Energy and Carbon, in the Construction Systems of Contemporary Quality Architecture. *Sustainability* **2019**, *11*, 3806. [CrossRef]
22. Agam, N.; Kustas, W.P.; Anderson, M.C.; Li, F.; Neale, C.M. A vegetation index based technique for spatial sharpening of thermal imagery. *Remote Sens. Environ.* **2007**, *107*, 545–558. [CrossRef]
23. Bisquert, M.; Sánchez-Tomás, J.M.; Caselles, V. Evaluation of Disaggregation Methods for Downscaling MODIS Land Surface Temperature to Landsat Spatial Resolution in Barrax Test Site. *IEEE J. Sel. Top. Appl. Earth Obs. Remote Sens.* **2016**, *9*, 1430–1438. [CrossRef]
24. Sattari, F.; Hashim, M.; Sookhak, M.; Banihashemi, S.; Pour, A.B. Assessment of the TsHARP method for spatial downscaling of land surface temperature over urban regions. *Urban Clim.* **2022**, *45*, 101265. [CrossRef]
25. Sobrino, J.A.; Raissouni, N.; Li, Z.-L. A Comparative Study of Land Surface Emissivity Retrieval from NOAA Data. *Remote Sens. Environ.* **2001**, *75*, 256–266. [CrossRef]
26. Wang, F.; Qin, Z.; Song, C.; Tu, L.; Karnieli, A.; Zhao, S. An Improved Mono-Window Algorithm for Land Surface Temperature Retrieval from Landsat 8 Thermal Infrared Sensor Data. *Remote Sens.* **2015**, *7*, 4268–4289. [CrossRef]
27. Available online: https://posit.co/ (accessed on 10 March 2020).
28. Available online: https://qgis.org/en/site/ (accessed on 24 April 2021).
29. Jiménez-Muñoz, J.C.; Sobrino, J.A.; Skoković, D.; Mattar, C.; Cristóbal, J. Land Surface Temperature Retrieval Methods From Landsat-8 Thermal Infrared Sensor Data. *IEEE Geosci. Remote Sens. Lett.* **2014**, *11*, 1840–1843. [CrossRef]
30. Available online: https://ladsweb.modaps.eosdis.nasa.gov (accessed on 14 December 2022).
31. ESA. Sentinel-2 User Handbook, Agence Spatiale Europeenne. 2015. Available online: https://sentinels.copernicus.eu/documents/247904/685211/Sentinel-2_User_Handbook.pdf/8869acdf-fd84-43ec-ae8c-3e80a436a16c?t=1438278087000 (accessed on 13 October 2021).
32. Available online: https://scihub.copernicus.eu/dhus/#/home (accessed on 13 October 2021).
33. Available online: https://earthexplorer.usgs.gov (accessed on 28 September 2021).
34. Price, J.C. Land surface temperature measurements from the split window channels of the NOAA 7 Advanced Very High Resolution Radiometer. *Atmospheres* **1984**, *89*, 7231–7237. [CrossRef]
35. Guillevic, P.; Göttsche, F.; Nickeson, J.; Hulley, G.; Ghent, D.; Yu, Y.; Trigo, I.; Hook, S.; Sobrino, J.; Remedios, J. Land Surface Temperature Product Validation Best Practice Protocol. In *Good Practices for Satellite-Derived Land Product Validation*; WGCV/CEOS, 2017; p. 60. Available online: https://lpvs.gsfc.nasa.gov/PDF/CEOS_LST_PROTOCOL_Feb2018_v1.1.0_light.pdf (accessed on 10 December 2023).
36. Yu, Y.; Liu, Y.; Yu, P.; Wang, H. *Enterprise Algorithm Theoretical Basis Document for Viirs Land Surface Temperature Production*; NOAA: Silver Spring, MD, USA, 2017.
37. Ahmed, S. Assessment of urban heat islands and impact of climate change on socioeconomic over Suez Governorate using remote sensing and GIS techniques. *Egypt. J. Remote Sens. Space Sci.* **2018**, *21*, 15–25. [CrossRef]
38. Hulley, G.C.; Hook, S.J.; Baldridge, A.M. ASTER land surface emissivity database of California and Nevada. *Geophys. Res. Lett.* **2008**, *35*, 165–174. [CrossRef]
39. Hulley, G.C.; Hook, S.J. The North American ASTER Land Surface Emissivity Database (NAALSED) Version 2.0. *Remote Sens. Environ.* **2009**, *113*, 1967–1975. [CrossRef]

40. Ding, Y.; Zheng, X.; Zhao, K.; Xin, X.; Liu, H. Quantifying the Impact of $NDVI_{soil}$ Determination Methods and $NDVI_{soil}$ Variability on the Estimation of Fractional Vegetation Cover in Northeast China. *Remote Sens.* **2016**, *8*, 29. [CrossRef]
41. Dymond, J.R.; Stephens, P.R.; Newsome, P.F.; Wilde, R.H. Percentage vegetation cover of a degrading rangeland from SPOT. *Int. J. Remote Sens.* **1992**, *13*, 1999–2007. [CrossRef]
42. Wan, Z.; Dozier, J. A generalized split-window algorithm for retrieving land-surface temperature from space. *IEEE Trans. Geosci. Remote Sens.* **1996**, *34*, 892–905. [CrossRef]
43. Ren, H.; Du, C.; Liu, R.; Qin, Q.; Yan, G.; Li, Z.; Meng, J. Atmospheric water vapor retrieval from Landsat 8 thermal infrared images. *J. Geophys. Res. Atmos.* **2015**, *120*, 1723–1738. [CrossRef]
44. Ren, H.; Dong, J.; Liu, R.; Zheng, Y.; Guo, J.; Chen, S.; Nie, J.; Zhao, Y. New hybrid algorithm for land surface temperature retrieval from multiple-band thermal infrared image without atmospheric and emissivity data inputs. *Int. J. Digit. Earth* **2020**, *13*, 1430–1453. [CrossRef]
45. Meng, X.; Cheng, J.; Zhao, S.; Liu, S.; Yao, Y. Estimating Land Surface Temperature from Landsat-8 Data using the NOAA JPSS Enterprise Algorithm. *Remote Sens.* **2019**, *11*, 155. [CrossRef]
46. Du, C.; Ren, H.; Qin, Q.; Meng, J.; Zhao, S. A Practical Split-Window Algorithm for Estimating Land Surface Temperature from Landsat 8 Data. *Remote Sens.* **2015**, *7*, 647–665. [CrossRef]
47. Gerace, A.; Kleynhans, T.; Eon, R.; Montanaro, M. Towards an Operational, Split Window-Derived Surface Temperature Product for the Thermal Infrared Sensors Onboard Landsat 8 and 9. *Remote Sens.* **2020**, *12*, 224. [CrossRef]
48. Coll, C.; Caselles, V. A split-window algorithm for land surface temperature from advanced very high resolution radiometer data: Validation and algorithm comparison. *Atmospheres* **1997**, *102*, 16697–16713. [CrossRef]
49. Kerr, Y.H.; Lagouarde, J.P.; Imbernon, J. Accurate land surface temperature retrieval from AVHRR data with use of an improved split window algorithm. *Remote Sens. Environ.* **1992**, *41*, 197–209. [CrossRef]
50. McClain, E.P.; Pichel, W.G.; Walton, C.C. Comparative performance of AVHRR-based multichannel sea surface temperatures. *J. Geophys. Res. Ocean.* **1985**, *90*, 11587–11601. [CrossRef]
51. Price, J.C. Estimating surface temperatures from satellite thermal infrared data—A simple formulation for the atmospheric effect. *Remote Sens. Environ.* **1983**, *13*, 353–361. [CrossRef]
52. Sobrino, J.A.; Caselles, V.; Coll, C. Theoretical split-window algorithms for determining the actual surface temperature. *Il Nuovo Cimento C* **1993**, *16*, 219–236. [CrossRef]
53. Ulivieri, C.; Castronuovo, M.M.; Francioni, R.; Cardillo, A. A split window algorithm for estimating land surface temperature from satellites. *Adv. Space. Res.* **1994**, *14*, 59–65. [CrossRef]
54. Liang, S. Narrowband to broadband conversions of land surface albedo I: Algorithms. *Remote Sens. Environ.* **2001**, *76*, 213–238. [CrossRef]
55. *T. 20701-1*; Analytical National Standards of Parameters of Estimating Building Energy Performance Energy Class Certificate Production. Technical Chamber of Greece: Athens, Greece, 2017.
56. Hendel, M.; Parison, S.; Grados, A.; Royon, L. Which pavement structures are best suited to limiting the UHI effect? A laboratory-scale study of Parisian pavement structures. *J. Affect. Disord.* **2018**, *144*, 216–229. [CrossRef]
57. Chatzidimitriou, A.; Yannas, S. Microclimate development in open urban spaces: The influence of form and materials. *Energy Build.* **2015**, *108*, 156–174. [CrossRef]

Disclaimer/Publisher's Note: The statements, opinions and data contained in all publications are solely those of the individual author(s) and contributor(s) and not of MDPI and/or the editor(s). MDPI and/or the editor(s) disclaim responsibility for any injury to people or property resulting from any ideas, methods, instructions or products referred to in the content.